

THE PENNSYLVANIA STATE UNIVERSITY
SCHREYER HONORS COLLEGE

DEPARTMENT OF MECHANICAL AND NUCLEAR ENGINEERING

THE ONSET OF VORTEX BREAKDOWN IN SWIRLING, TURBULENT JETS

SEAN CLEES
SPRING 2018

A thesis
submitted in partial fulfillment
of the requirements
for a baccalaureate degree
in Nuclear Engineering
with honors in Mechanical Engineering

Reviewed and approved* by the following:

Jacqueline O'Connor
Assistant Professor of Mechanical Engineering
Thesis Supervisor and Honors Adviser

Rui Ni
Kenneth Kuan-Yun Kuo Early Career Professor
Assistant Professor of Mechanical Engineering
Faculty Reader

* Signatures are on file in the Schreyer Honors College.

ABSTRACT

Swirling jets are commonly used in combustion applications to stabilize flames and improve emissions. Thus, their dynamics play an important role in combustor design. Despite the prevalence of swirling flows in industrial applications that involve highly turbulent flow fields, the majority of experimental and numerical studies consider only laminar conditions. In this study, the dynamics of the vortex core are investigated in a swirling, turbulent jet at swirl numbers in the range of the critical swirl number for vortex breakdown. Vortex breakdown, a bifurcation in the structure of a swirling jet, results in the establishment of a stagnation point and recirculation region along the centerline of the jet. To study these dynamics, dynamic mode decomposition, an order-reduction technique used to extract coherent structures from flow data, is implemented. Investigation of time-averaged velocity fields and profiles leads to the identification of three flow regimes: pre-breakdown, near-breakdown, and post-breakdown. Velocity fields in these regimes are further analyzed using dynamic mode decomposition, Rankine-vortex fitting, and proper orthogonal decomposition to characterize jet dynamics with a particular focus on the development of the recirculation region characteristic of vortex breakdown. A precessing vortex core is also identified in the post-breakdown regime and its behavior is discussed.

TABLE OF CONTENTS

LIST OF FIGURES.....	iii
LIST OF TABLES.....	iv
ACKNOWLEDGEMENTS.....	v
Chapter 1 Introduction	1
1.1 Motivation	1
1.2 Swirl Background.....	4
1.3 General Dynamics of Swirling Flows	4
1.4 Vortex Breakdown Structure	6
1.5 Theories of Vortex Breakdown	8
1.6 Predicting Vortex Breakdown	9
1.7 Vortex Breakdown in Turbulence	10
Chapter 2 Experimental Configuration	11
2.1 Combustor Facility	11
2.2 Particle Image Velocimetry Setup.....	13
Chapter 3 Dynamic Mode Decomposition	15
3.1 Mathematical Background.....	15
3.2 Truncation	20
3.3 Validation	21
Chapter 4 Time-Averaged Results.....	28
Chapter 5 Flow Dynamics	31
5.1 Pre-Breakdown Regime.....	32
5.2 Near-Breakdown Regime	33
5.3 Post-Breakdown Regime	42
Chapter 6 Conclusions and Future Work.....	48
BIBLIOGRAPHY	50
Appendix A Dynamic Mode Decomposition Code	53
Appendix B Synthetic Data Code	64

LIST OF FIGURES

Figure 1. Schematic of a flame stabilized in a swirling flow as found in a gas turbine combustor.	2
Figure 2. Visualization of a swirling jet in water exhibiting flow recirculation along the jet centerline characteristic of vortex breakdown [3].	3
Figure 3. Visualization of a laminar swirling jet at a) $S = 0$ and b) $S = 0.44$ [5].	5
Figure 4. Visualization of a) spiral breakdown, b) helical breakdown, and c) axisymmetric breakdown in laminar pipe flow [9].	7
Figure 5. Experimental facility with two-microphone nozzle (upper right) and swirler casing (lower right).	12
Figure 6. Sample mode shapes for a) 100 Hz and b) 300 Hz modes from the first validation test without Gaussian noise.	24
Figure 7. DMD spectrum for first validation case without Gaussian noise. Circles indicate modes at the prescribed perturbation frequencies.	26
Figure 8. Time-averaged axial velocity fields for each swirl number of interest.	28
Figure 9. Average axial velocity profiles for swirl numbers of interest at $x/D = 1$.	29
Figure 10. Time-averaged azimuthal vorticity fields for each swirl number.	30
Figure 11. DMD mode spectra for a) $S = 0$ and b) $S = 0.18$. Dot color is representative of mode coherence. Circled modes are shown in Figure 12 and Figure 13.	32
Figure 12. Notable axial modes for $S = 0$ showing a) axisymmetric behavior at 650 Hz and b) axial vortex roll-up at 735 Hz.	33
Figure 13. 792 Hz mode showing the tilting of axial Kelvin-Helmholtz vortices due to introduction of swirl at $S = 0.18$. White lines connect the centers of corresponding vortices.	33
Figure 14. Axial and radial velocity fluctuations for $S = 0.38$, normalized by bulk velocity: a) unfiltered fluctuations, b) low-pass filtered with 150 Hz cutoff, and c) high-pass filtered with 150 Hz cutoff. Blue (black) coloration indicates positive (negative) radial fluctuation and red (cyan) coloration indicates positive (negative) axial fluctuation.	35
Figure 15. DMD modes for a) $S = 0.38$ and b) $S = 0.46$. Circled modes shown in Figure 11 and Figure 10.	36
Figure 16. 560 Hz mode showing the emergence of central shear layer at $S = 0.38$.	36
Figure 17. Coherent axisymmetric response at 265 Hz at $S = 0.46$.	37
Figure 18. Examples of mean radial velocity distributions: a) $S = 0.46$, b) $S = 0.66$.	37

Figure 19. Top view of a snapshot of the vortex core location, blue to red denotes increasing x/D from 0 to 3.....	39
Figure 20. Perspective view of the vortex core location as for Figure 19, green to blue denotes decreasing vortex intensity.....	39
Figure 21. PDFs of vortex core locations at two axial locations: a) $x/D = 0.122$, b) $x/D = 2.316$	40
Figure 22. Mean location (r/D , z/D) and size of the vortex core (R/D) as function of axial distance (x/D): a) $S = 0.38$, and b) $S = 0.46$	41
Figure 23. Cross-correlation sequence of the radial velocity field with the z -coordinate of the vortex core (reference signal) at the location marked by the red marker for $S = 0.38$. Lag increases from upper left to lower right.	42
Figure 24. Axial and radial velocity fluctuations for $S = 0.56$, normalized by bulk velocity: a) unfiltered fluctuations, b) low-pass filtered with 150 Hz cutoff, and c) high-pass filtered with 150 Hz cutoff. Blue (black) coloration indicates positive (negative) radial fluctuation and red (cyan) coloration indicates positive (negative) axial fluctuation.	43
Figure 25. DMD mode spectra for a) $S = 0.56$ and b) $S = 0.66$. Circled modes are shown in Figure 26 and Figure 27.	44
Figure 26. Emergence of highly damped PVC-like dynamics in 884 Hz mode at $S = 0.56$; a) radial mode, b) axial mode, c) azimuthal mode.	45
Figure 27. Clearer PVC present in 858Hz mode at $S = 0.66$; a) radial mode, b) axial mode, c) azimuthal mode.	45
Figure 28. Radial POD modes 7-10 for $S = 0.66$	46
Figure 29. Pressure spectra for $S = 1.05$ case where a strong PVC is present (black) and $S = 0.66$ case featuring weak PVC (red).	47

LIST OF TABLES

Table 1. Swirler angles of interest and corresponding geometric swirl numbers.	13
Table 2. Swirl numbers and corresponding DMD truncation parameters.....	21

ACKNOWLEDGEMENTS

First and foremost, I would like to thank Dr. Jacqueline O'Connor for her scientific, professional, and personal guidance throughout my time in the Reacting Flow Dynamics Laboratory. Working with Dr. O'Connor has opened my eyes to the world of academic research, and through that research I have found my drive and passion. Dr. O'Connor, these few words cannot hope to express the gratitude I feel for everything you have done for me over the past few years. I truly could not have asked for a better mentor.

I would like to thank Dr. Jacques Lewalle for his significant contribution to the content of this work. I am grateful for the opportunity to have collaborated with such a respected researcher, and I am greatly appreciative of all that you taught me throughout our collaboration.

Next, I would like to acknowledge my fellow undergraduate researchers on the swirl project, Mark Frederick and Danielle Mason. This work has truly been a team effort and you helped make it rewarding and fun. I would also like to extend my thanks to Wyatt Culler, Dr. Anand Makwana, Dr. Stephen Peluso, and Ankit Tyagi for their support on this work, both technical and otherwise. My time in the Reacting Flow Dynamics Laboratory would not have been the same without such a fantastic group of researchers and friends to support me.

Above all, I would like to thank my family and friends for their constant support throughout my academic career thus far. None of my successes would have been possible without my fantastic support group. To my parents, thank you for giving me the freedom and opportunity to pursue my academic goals. Your constant support means the world to me.

Finally, I would like to acknowledge the Erickson Discovery Grant program at Penn State for funding me to conduct this research during the summer of 2017.

Chapter 1

Introduction

1.1 Motivation

The modern age has been characterized by an ever-increasing demand for energy, in all its forms. Today, gas turbines play an important role in fulfilling this need, providing both propulsion for air and sea transport and electric power for homes and industry. Of late, concerns over man-made climate change have spurred innovations in gas turbine technology. Cutting-edge designs focus on maximizing efficiency while reducing the production of pollutants such as carbon monoxide (CO), nitric oxides (NO_x), and unburnt hydrocarbons (UHC). These gaseous products of the combustion process are of particular concern due to their contribution to the greenhouse effect and acid rain [1]. With the recent emergence of natural gas as the primary source of power in the United States [2], the need for efficiency and cleanliness has only increased. In order for innovation to take place, designers must have access to extensive knowledge of the underlying physical phenomena that take place in gas turbine engines.

In particular, the aerodynamics of gas turbine engines are critical to accomplishing these low-emissions, high-efficiency design goals. The focus of the work in this thesis is flow inside the combustor, which is the region of the engine where heat is added through the chemical conversion of fuel and air to products and heat. In gas turbine combustors, swirling flows are commonly employed as a means of managing the combustion process. Importantly, these flows provide for improved flame stability and enhanced fluid mixing within the combustor due to

strong flow recirculation [1]. Because of the geometry of swirling jets under certain conditions, flames become rooted in place at the center of the flow, as seen in the schematic in Figure 1.

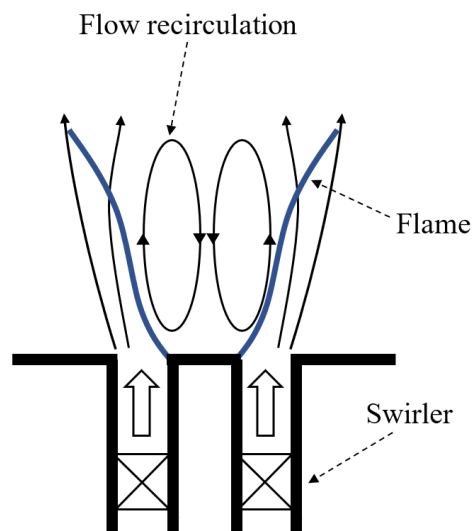


Figure 1. Schematic of a flame stabilized in a swirling flow as found in a gas turbine combustor.

This behavior allows for precise control of flame shape and position, allowing designers to fine-tune flames for efficiency and lower emissions. In addition, swirling flows encourage the mixing of unburnt fuel and fresh air with hot, volatile combustion products, particularly in turbulent flow fields that already provide for enhanced mixing over laminar flows. This mixing also improves combustion efficiency by allowing for more complete combustion, reducing the emissions of unburnt hydrocarbons in the process.

It is clear that swirling flows are a crucial tool for controlling combustion in gas turbines, and it is in fact their inherent instability that makes them useful. Swirling flows undergo drastic changes in flow behavior and geometry, or bifurcations, as flow conditions are altered. One of these bifurcations, vortex breakdown, is of particular importance in the context of combustion. As the amount of swirl in a jet increases from zero and reaches a critical value, a region of

stagnation or reverse flow is formed along its centerline, as seen in the center of Figure 2. It is this phenomenon that provides for the improved flame stability and enhanced mixing that make swirling flows so useful.

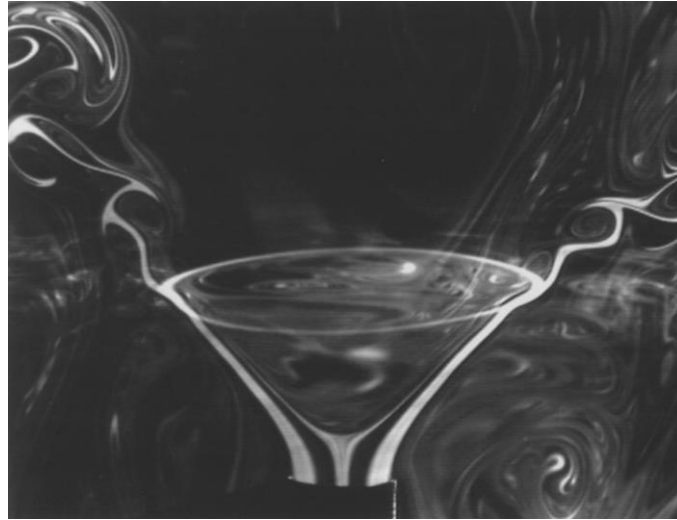


Figure 2. Visualization of a swirling jet in water exhibiting flow recirculation along the jet centerline characteristic of vortex breakdown [3].

While the effects of vortex breakdown are commonly leveraged in modern turbine combustor designs, the behavior of the bifurcation at gas-turbine-like conditions is poorly understood. Thus, it is the goal of this work to better understand the transition of a *turbulent* swirling jet to vortex breakdown. First, the current understanding of swirling jets and vortex breakdown is reviewed. In Chapter 2, the experimental facility and diagnostics used in this work are discussed. Chapter 3 details the theory, application, and validation of dynamic mode decomposition, the primary analytical tool used in this study. In Chapter 4, the flow fields under consideration are analyzed from a time-averaged perspective. Flow dynamics are discussed in Chapter 5, with a particular focus on the application of dynamic mode decomposition and the analysis of vortex core motion. Finally, Chapter 6 summarizes the conclusions and suggests future work.

1.2 Swirl Background

Swirling jets are generally described by their swirl number, S , a non-dimensional quantity that describes the amount of swirl in the flow. Generally, S is defined as the ratio of the axial flux of azimuthal momentum and the axial flux of axial momentum:

$$S = \frac{\int_0^R \rho u_x u_\theta r^2 dr}{R \int_0^R \rho u_x^2 r dr} \quad (1.1)$$

where R is the outer radius of the jet, ρ is the density of the fluid, u_x is the axial velocity, u_θ is the azimuthal velocity, and r is the radial distance from the center of the jet [4]. A global value for swirl number can be difficult to calculate using this formulation due to its strong dependence on the location in the jet at which the calculation is performed. Thus, in order to describe overall jet behavior, geometric swirl number is used. The geometric swirl number is based purely on the geometry of the swirler used to generate the swirling jet, and thus is a more general way to quantify swirl. All values of S reported in this work are geometric swirl number based on the swirler design described in Chapter 2.

1.3 General Dynamics of Swirling Flows

Non-swirling and low-swirl jets prior to the onset of vortex breakdown exhibit a wide range of dynamics. In their laminar study, Liang and Maxworthy [5] found that non-swirling jets ($S = 0$) are dominated by axisymmetric coherent structures that develop due to an axial Kelvin-Helmholtz instability. This instability generates axisymmetric vortex rings that roll up in the outer shear layers as they are convected downstream. As they propagate, these vortices tend to pair, leading to increased size and decreased shedding frequency, until the jet eventually decays

into fully-developed turbulence and individual coherent structures are unrecognizable. At low levels of swirl ($0 < S < 0.60$), Liang and Maxworthy observed that these axisymmetric vortex rings begin to tilt as they convect due to the loss of symmetry. In addition, the presence of azimuthal shear generates azimuthal instabilities that manifest as co-rotating but counter-winding vortex tubes. At low swirl, these azimuthal vortices are dominated by the axisymmetric (or eventually tilted) rings, but they become dominant as swirl is increased.

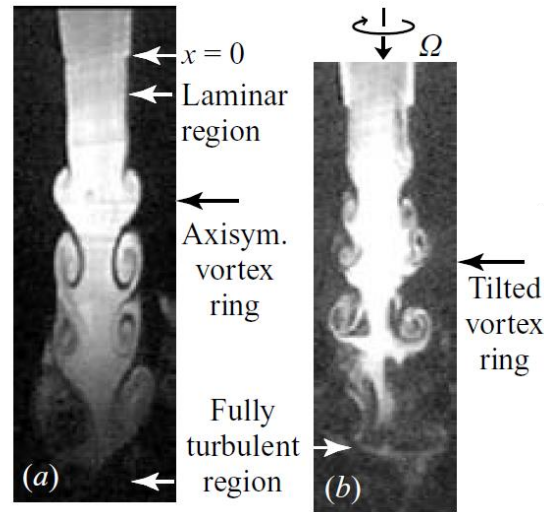


Figure 3. Visualization of a laminar swirling jet at a) $S = 0$ and b) $S = 0.44$ [5].

The coherent structures present in swirling jets are largely created by hydrodynamic instabilities in the flow. In their numerical study, Gallaire and Chomaz [6] identified two instability mechanisms that contribute to the presence of azimuthal vortices in swirling jets: azimuthal Kelvin-Helmholtz and centrifugal. Both of these instabilities are present in the swirling jet due to the presence of azimuthal shear, though their mechanisms differ significantly. The Kelvin-Helmholtz instability is driven by a pressure differential across a boundary layer between two fluids moving at different velocities. Disturbances within this boundary layer due to turbulence, interactions with the nozzle exit, etc. displace fluid packets towards or away from

the jet core. As fluid is displaced away from the vortex core, the streamlines within the core expand, indicating deceleration and higher pressure, while those outside of the core contract, indicating acceleration and decreased pressure. This pressure differential causes the initial disturbance to grow and thus it is termed an instability. This mechanism is identical to the axial Kelvin-Helmholtz mechanism that generates the axisymmetric and tilted vortex rings that dominate in non-swirling and low-swirl jets.

Centrifugal instability is also driven by the presence of shear, though it is unique to azimuthal shear and does not contribute to axial instability. Within the swirling jet, the increased azimuthal velocity leads to a larger centrifugal force than in the surrounding fluid. This centrifugal force is balanced by a radial pressure gradient, which is also larger inside the jet than outside. Disturbances within the boundary layer between the quickly-rotating jet and the slowly-rotating surrounding fluid displace fluid towards or away from the jet core. As fluid packets from the core are displaced into the surrounding fluid, they experience a smaller radial pressure gradient that is insufficient to balance the centrifugal force they experience and thus are accelerated outwards. Likewise, as fluid packets from the surrounding fluid are displaced towards the core, they experience a larger pressure gradient that is not balanced by the centrifugal force they experience and are thus accelerated inwards. Thus, the initial disturbance is unstable and grows into a vortex structure.

1.4 Vortex Breakdown Structure

The vortex breakdown (VB) phenomenon was first identified and documented by Peckham and Atkinson [7] in flow over delta wings. Generally, the structure of VB was

described as if a body had been placed along the axis of the vortex, causing fluid to flow around it and creating a wake-like flow pattern along the jet centerline. This body takes the form of a hemispherical bubble of nearly-stagnant or recirculating fluid downstream of a stagnation point.

Harvey [8] further examined the VB phenomenon in swirling laminar pipe flow, in which the hemispherical bubble was found to close completely into an elongated sphere. In this flow geometry, two stagnation points were observed: one at the upstream edge of the VB bubble and one at the downstream edge. Downstream of this breakdown bubble, the flow returned to a similar state as upstream of the VB bubble.

Extensive studies on VB in a tube conducted by Sarpkaya [9] initially identified three unique varieties of VB in laminar flows: spiral breakdown (Figure 4a), helical breakdown (Figure 4b), and axisymmetric breakdown (Figure 4c). In later turbulent studies, Sarpkaya [10] identified a fourth type of VB, conical vortex breakdown, which manifested as a turbulent, conical, wake-like structure emanating from behind a stagnation point. This is the type of VB that appears in the majority of engineering applications.

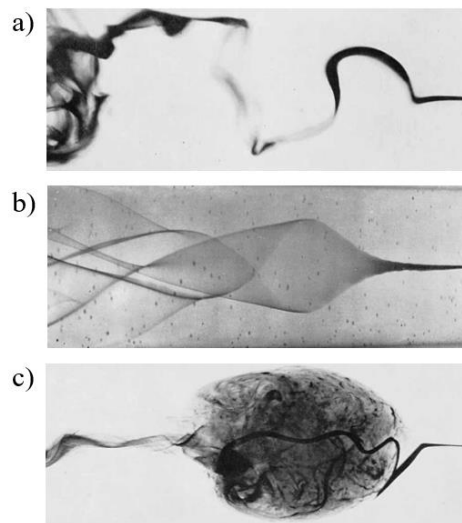


Figure 4. Visualization of a) spiral breakdown, b) helical breakdown, and c) axisymmetric breakdown in laminar pipe flow [9].

Billant *et al.* [3] extensively characterized vortex breakdown in a free swirling jet.

Vortex breakdown was found to occur at a critical level of swirl, S_c , which depended on nozzle geometry and Reynolds number. As S was increased and approached S_c , a stagnation point appeared in the turbulent region of the jet and moved upstream until reaching a fixed position. Billant *et al.* identified four distinct forms of VB that developed following the formation of this stagnation point: bubble, cone, asymmetric bubble, and asymmetric cone. The bubble was similar in appearance to the asymmetric VB observed by Sarpkaya [10], and the cone can be seen in Figure 2. The asymmetric varieties of these structures consist of a precession of the stagnation point about the jet centerline. Notably, hysteretic behavior was observed: both forms of VB were observed at the same flow conditions.

1.5 Theories of Vortex Breakdown

Since the first observation of the VB phenomenon, a number of theories have been developed to explain the flow bifurcation. Based on experimental work by Harvey, Benjamin [8, 11] proposed and later developed a theory of VB that explained the phenomenon as a finite transition between supercritical and subcritical states. When the flow is supercritical, *i.e.* upstream of the VB structure, infinitesimal perturbations cannot propagate upstream and thus the flow cannot sustain standing waves. However, analogous to a hydraulic jump in channel flow, the flow can transition to a subcritical state in which infinitesimal perturbations can propagate upstream and downstream, allowing standing waves to form and generating VB.

A competing theory, proposed by studied experimentally by Escudier *et al.* [12], suggested that VB was a result of the hydrodynamic stability of the swirling jet to non-

axisymmetric disturbances. Escudier *et al.* examined confined swirling jets within the context of both theories and found merits to both. When VB was observed, the flow was found to be both critical and unstable to non-axisymmetric disturbances, suggesting that VB is explained by a more subtle interaction between the theories. In addition, Escudier *et al.* observed flows that were unstable but did not feature VB, again suggesting that both stability and criticality must be considered to understand the phenomenon.

Theoretical work by Healey [13] sought to reconcile the finite transition and hydrodynamic stability theories under the more recent conceptual framework of convective and absolute instability. Convective instabilities, such as the Kelvin-Helmholtz and centrifugal instabilities discussed above, develop only downstream as they are convected away. Absolute instabilities, however, grow rapidly enough to develop both upstream and downstream, eventually coming to dominate the flow structure. Within this framework, Healey explained that the theories of Benjamin and Ludwig are essentially describing the same phenomenon in two different ways. Thus, according to Healey, VB can be explained as a transition from convective instability to absolute instability. [13]

1.6 Predicting Vortex Breakdown

Linear stability analysis is a common tool used to predict the stability of flows to perturbations. The technique has been applied to swirling jets near VB, notably by Loiseleux, Chomaz, and Huerre [14]. In this study, a Rankine vortex model was perturbed with axisymmetric and non-axisymmetric ansatzes and the growth of these perturbations was calculated by solving a dispersion relation derived from the linearized Navier-Stokes equations.

This analysis showed that as swirl is increased, swirling jets become absolutely unstable to axisymmetric motions first, but this instability is almost immediately overtaken by antisymmetric and then by helical motions. This transition to absolute instability occurred at a swirl number of $S = 0.43$, which agrees generally with experimental results. Notably, counter-winding motions (*i.e.* helices that wind opposite the direction of net swirl) were found to be always less stable than their co-winding counterparts. In addition, this study was conducted without any turbulence model included in the linearized Navier-Stokes equations.

1.7 Vortex Breakdown in Turbulence

While VB is most commonly applied in highly turbulent conditions, such as gas turbine combustors, relatively little work has been done on VB in turbulent flows. Aside from Sarpkaya's later work on turbulent VB [10], all of the experiments discussed thus far were conducted under laminar flow conditions. In addition, little work has been done to understand the linear stability of swirling jets while incorporating turbulence effects. Recent work by Rukes *et al.* [15] and Frederick *et al.* [16] has begun to implement turbulence models into the considered Navier-Stokes equations, but few extensive studies exist that focus on the onset of VB from a linear stability perspective while considering turbulence. The lack of both experimental and computational studies that treat VB in turbulent conditions calls for additional investigation and motivates this work.

Chapter 2

Experimental Configuration

2.1 Combustor Facility

To study turbulent swirling flows, an experimental facility was constructed previously to mimic the design of a gas turbine combustor. The facility, shown in Figure 5, consists of three main sections: a settling chamber, a variable-angle, radial-entry swirler (lower right in Figure 5), and an injector nozzle (upper right in Figure 5). First, incoming air enters the 15.25 cm-diameter settling chamber at the base of the facility through a 5.08 cm-diameter hose and passes through two perforated plates. These plates reduce the impact of any large-scale eddies that may form upstream of the facility itself. The settling chamber is fitted with a pair of 100 W sirens (Galls Model SK144) that can be used to provide longitudinal acoustic forcing, though they are not used for the purposes of this work.

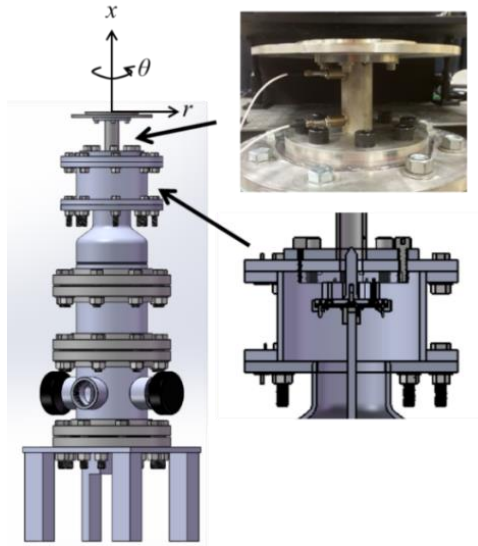


Figure 5. Experimental facility with two-microphone nozzle (upper right) and swirler casing (lower right).

After passing through the settling chamber, air flows upwards to the variable-angle, radial-entry swirler. The swirler consists of eight NACA 0025 airfoil blades mounted around a centerbody. Each airfoil has a height and chord length of 2.54 cm. The trailing edge of each airfoil is secured to the top and bottom of the swirler by a pin about which the airfoil can pivot. A pin close to the leading edge of each blade passes through a curved slot in the base of the swirler and is held by a separate plate below. This lower plate is fastened to a shaft that can be turned by a stepper motor attached beneath the settling chamber. By turning this plate, the angle of the airfoil blades can be adjusted between 65° and -65° with a resolution of 2.5° . This angle is set by visually inspecting the swirler through holes that are plugged during operation. A positive blade angle results in a jet that swirls counter-clockwise, and a negative angle results in a jet that swirls clockwise. Thus, as per the coordinate system defined in Figure 5, positive angles produce positive azimuthal velocity and negative angles produce negative azimuthal velocity.

A centerbody in the swirler redirects flow upwards into the injector nozzle and tapers to a point 8.9 cm upstream of the nozzle exit. Within the 2.54 cm-diameter nozzle, flow passes two

differential pressure transducers (PCB Model 113B28). These transducers are mounted 6.92 cm and 1.84 cm upstream of the nozzle exit, which corresponds to 2.54 cm and 7.62 cm downstream of the swirler, respectively. Flow exits the facility into the ambient air as an unconfined jet. For all cases considered in this work, the volumetric flow rate is maintained at 30 SCFM with a maximum deviation of 0.5 SCFM. This results in a calculated bulk flow velocity of 28 m/s and a Reynolds number of 35,000 based on the nozzle diameter. The volumetric flow rate is monitored using a thermal mass flow meter (Thermal Instruments Model 600-9). Signals from the flow meter and pressure transducers are sampled at 20 kHz for 3 seconds using a National Instruments CompactRIO system operating as a field-programmable gate array (FPGA).

Six levels of swirl are examined in this work, corresponding to airfoil blade angles of 0°, 15°, 30°, 35°, 40° and 45°. The level of swirl is quantified based on geometric swirl number, S , as defined by Lefebvre [1]; the relationship between angle and swirl number is listed in Table 1.

Table 1. Swirler angles of interest and corresponding geometric swirl numbers.

Swirler Angle (°)	Geometric Swirl Number
0	0.00
15	0.18
30	0.38
35	0.46
40	0.56
45	0.66

2.2 Particle Image Velocimetry Setup

Stereo particle image velocimetry (PIV) is used to measure three components of the velocity field in a plane that bisects the injector nozzle. In this r - x plane, with coordinate axes as shown in Figure 5, radial and axial velocities are in-plane and azimuthal velocity is out-of-plane. PIV images are captured by two Photron SA5 CMOS high-speed cameras in double-frame mode.

The cameras are arranged in a forward-forward configuration and are equipped with Scheimpflug adapters. Images are taken at 5 kHz with a variable interframe time of 17 – 23 μ s depending on the swirl number. A Hawk/Darwin Duo Nd-YAG, 532 nm, 60 W laser is used to illuminate the motion of aluminum oxide tracer particles, which are injected into the flow upstream of the settling chamber. These particles have a nominal diameter of 1 – 2 μ m and can accurately follow flow perturbations up to 4000 Hz.

Velocity fields are calculated in DaVis 8.3.1 from LaVision. Multi-pass cross correlation is conducted without pre-processing or masking. A 32x32 pixel interrogation window with 50% overlap is used in the first pass and two subsequent passes are made using a 16x16 pixel window, also with 50% overlap. Spurious vectors are identified and rejected using two separate methods during post-processing. First, a vector is removed and replaced via interpolation if its magnitude is greater than 3 times the RMS of the surrounding vectors. Second, DaVis employs universal outlier detection to identify and replace outlying vectors.

Chapter 3

Dynamic Mode Decomposition

The study of fundamental fluid dynamics commonly requires the identification of organized, large-scale flow features known as coherent structures [17]. A variety of methods exist for extracting these structures from experimental PIV data. Among these methods are a variety of decomposition techniques that exploit the recurring, often periodic nature of coherent structures to identify distinct motions in the flow, known as modes. Perhaps the most common flow field decomposition technique, proper orthogonal decomposition (POD), is key to this work, but much of the analysis relies more heavily on the use of a similar technique, dynamic mode decomposition (DMD). DMD was introduced to the field of fluid mechanics by Schmid [18] as an alternative to classical POD, and its unique capabilities have popularized the technique as a method of identifying coherent structures. This chapter discusses the mathematical background of DMD, one of the intricacies of implementing it as a data-analysis technique, and the process by which the DMD algorithm was validated using synthetic data. The MATLAB codes that were developed for DMD and generating synthetic data are included in Appendix A and Appendix B, respectively.

3.1 Mathematical Background

As with POD, DMD relies heavily on the principles of linear algebra to decompose a given time series of velocity fields into a number of spatial basis functions. In the case of DMD,

these spatial basis functions, $\boldsymbol{\psi}_k$, each oscillate at their own distinct complex frequency, ω_k . That each DMD mode is associated with a single complex frequency, itself containing a real frequency and a growth rate, is a key distinction between DMD and POD. POD modes are orthogonal in space; they each contain distinct spatial information but many frequencies. DMD modes are orthogonal in time; they represent dynamics occurring at one single frequency but they may not be spatially distinct from each other. The following algorithm, except where noted, is adapted from work by Schmid [18, 19] and Tu *et al* [20].

At its core, DMD relies on the assumption that there exists an operator, \mathbf{A} , that linearly maps each sequential state, or “snapshot,” onto the next. In this case, each of these snapshots is a single PIV frame. Under this assumption, the operator \mathbf{A} , known as the Koopman operator, describes all of the dynamics that govern the flow. For linear systems, the Koopman operator is a finite-dimensional operator that can, in theory, be directly calculated. However, for nonlinear systems, \mathbf{A} is an infinite-dimensional operator that cannot be written explicitly. The DMD algorithm is essentially an optimized least-squares approximation of the eigenmodes of this infinite-dimensional Koopman operator. For the purposes of DMD, the Koopman operator, \mathbf{A} , is defined as operating on some snapshot \mathbf{x}_t at time t to give the next sequential snapshot, \mathbf{x}_{t+1} , such that

$$\mathbf{x}_{t+1} = \mathbf{A}\mathbf{x}_t. \quad (3.1)$$

These K sequential snapshots, each separated by a constant time step Δt , are arranged as columns in a data matrix, \mathbf{X}_1^K , where

$$\mathbf{X}_1^K = \{\mathbf{x}_1, \mathbf{x}_2, \mathbf{x}_3, \dots, \mathbf{x}_K\}. \quad (3.2)$$

According to the notation \mathbf{X}_p^q above, p is the index of the first snapshot in the sequence and q is the index of the last snapshot. Given the definition in Equation 3.2, Equation 3.1 can be rewritten thusly:

$$\mathbf{X}_2^K = \mathbf{A}\mathbf{X}_1^{K-1}. \quad (3.3)$$

Equation 3.3 is the matrix generalization of Equation 3.1. The operator \mathbf{A} acts on each column of the data matrix \mathbf{X}_1^{K-1} , transforming each respective column into the next in the sequence of snapshots. Thus, Equation 3.3 can be understood as the operator \mathbf{A} transforming a matrix of all snapshots but the last into a matrix of all snapshots but the first. To approximate \mathbf{A} , Schmid assumes that, with enough snapshots, the vectors given by Equation 3.1 will be linearly dependent. Thus, the goal of DMD is to express the final snapshot in the sequence, \mathbf{x}_K , as a linear combination of the previous vectors up to $K - 1$. To this end, as per Schmid, Equation 3.3 can be rewritten in terms of a companion matrix, \mathbf{S} , of the form

$$\mathbf{S} = \begin{pmatrix} 0 & & & a_1 \\ 1 & 0 & & a_2 \\ & \ddots & \ddots & \vdots \\ & & 1 & 0 \\ & & & 1 & a_{K-1} \end{pmatrix}, \quad (3.4)$$

in which the constants a_k for $k = 1, \dots, K - 1$ are unknown and represent the linear combination of the first $K - 1$ snapshots necessary to form the K th snapshot. Thus, Equation 3.3 becomes

$$\mathbf{X}_2^K = \mathbf{A}\mathbf{X}_1^{K-1} = \mathbf{X}_1^{K-1}\mathbf{S} + \mathbf{r}\mathbf{e}_{K-1}^T, \quad (3.5)$$

where \mathbf{r} is a vector of residuals and \mathbf{e}_{K-1} is the $(K - 1)$ th unit vector. The eigenvalues and eigenvectors of \mathbf{S} approximate those of \mathbf{A} , and can be computed directly at this stage after the constants a_k are calculated using a QR decomposition of the data matrix, $\mathbf{X}_1^{K-1} = \mathbf{Q}\mathbf{R}$:

$$\mathbf{a} = \mathbf{R}^{-1}\mathbf{Q}^*\mathbf{x}_K. \quad (3.6)$$

The application of DMD to experimental data requires additional care due to the presence of noise and, in the present study, turbulence. To achieve a more robust DMD algorithm for the purposes of this study, a pre-processing step was used in order to eliminate low-energy flow behavior that could obscure any coherent structures that may be extracted via DMD. To identify low-energy behavior, POD was applied to the sequence of PIV snapshots prior to the application of DMD. This technique was derived from the higher-order DMD algorithm of Le Clainche, Vega, and coworkers [21, 22]. While these authors do not explicitly refer to their filtering method as POD-filtering, the connection between the two is clear in the implementation.

Prior to the approximation of \mathbf{A} , POD is applied to the data matrix \mathbf{X}_1^K via the singular value decomposition (SVD), such that $\mathbf{X}_1^K = \mathbf{U}\mathbf{\Sigma}\mathbf{V}^*$. The matrices \mathbf{U} and \mathbf{V} contain the spatial and temporal content, respectively, of the original data matrix. The diagonal matrix $\mathbf{\Sigma}$ contains the singular values, σ_k , of the data matrix. The square of these singular values is a measure of the fluctuating energy of the corresponding POD mode. To eliminate modes that contain noise and turbulence, the SVD is truncated, retaining N modes according to the relation given in Equation 3.7:

$$\frac{\sigma_{N+1}^2 + \dots + \sigma_K^2}{\sigma_1^2 + \dots + \sigma_K^2} \leq \epsilon_t, \quad (3.7)$$

where ϵ_t is the fraction of total turbulent kinetic energy that is contained in the removed modes, referred to as the “truncation parameter.” The selection of this truncation parameter is nontrivial and is discussed in further detail in the next section of this chapter. Using the results of the truncated SVD, a “reduced” snapshot matrix is calculated as

$$\hat{\mathbf{X}}_1^K = \hat{\mathbf{\Sigma}}\hat{\mathbf{V}}^*, \quad (3.8)$$

and it is this matrix that is used to compute the DMD modes. In order to approximate the companion matrix \mathbf{S} in Equation 3.5, new data matrices $\hat{\mathbf{X}}_1^{K-1}$ and $\hat{\mathbf{X}}_2^K$ are constructed. Returning to the DMD algorithm as initially described by Schmid, SVD is applied to the former data matrix, yielding $\hat{\mathbf{X}}_1^{K-1} = \mathbf{W}\mathbf{\Lambda}\mathbf{T}^*$. Thus, $\tilde{\mathbf{S}}$, a dimension-reduced approximation of \mathbf{A} , is be found as

$$\tilde{\mathbf{S}} = \mathbf{W}^* \hat{\mathbf{X}}_2^K \mathbf{T} \mathbf{\Lambda}^{-1}. \quad (3.9)$$

The eigenvalues and eigenvectors of \mathbf{A} are approximated by the eigenvectors, \mathbf{y}_m , and eigenvalues, μ_m , of $\tilde{\mathbf{S}}$, which are found by solving the standard eigenvalue problem

$$\tilde{\mathbf{S}}\mathbf{y}_m = \mu_m\mathbf{y}_m \text{ for } 1 \leq m \leq M, \quad (3.10)$$

where M is the total number of modes that result from DMD. Without any truncation, i.e. with $\epsilon_t = 0$, the algorithm always results in $M = K - 1$.

To construct the DMD modes, $\boldsymbol{\psi}_k$, the eigenvectors found above are projected back into the space of the original data matrix via Equation 3.11 and the corresponding eigenvalues are transformed into complex frequencies, ω_k , via Equation 3.12:

$$\boldsymbol{\psi}_k = \mathbf{U}\mathbf{W}\mathbf{y}_m, \quad (3.11)$$

$$\omega_k = \frac{\ln(\mu_k)}{\Delta t}. \quad (3.12)$$

The real parts of these complex frequencies are the temporal growth rates of each mode, and the imaginary parts are the corresponding frequencies. The initial amplitudes of each DMD mode, contained in the vector \mathbf{b} , can be calculated as

$$\mathbf{b} = \boldsymbol{\Psi}^+ \mathbf{x}_1, \quad (3.13)$$

where Ψ is the matrix containing all of the DMD modes, ψ_k , as columns and the superscript ‘+’ denotes the Moore-Penrose pseudoinverse. Thus, the original time series of PIV snapshots can be approximately reconstructed as a linear combination of the resulting DMD modes:

$$\mathbf{x}_{DMD}(t) = \sum_1^M b_m \psi_m \exp(\omega_m t). \quad (3.14)$$

3.2 Truncation

The truncation parameter, ϵ_t , as introduced in Equation 3.7, must be carefully selected in order to maintain the integrity of the final set of modes. Truncating too much could remove relevant physical motions, but truncating too little results in poor performance of the DMD algorithm and nonphysical results. According to Le Clainche and Vega [22], optimal DMD performance is achieved when the resulting number of modes, M , is equal to the dimension of the subspace spanned by the modes, N . The value of N can be calculated simply by finding the rank of the matrix containing all of the resulting modes, Ψ . The values M and N are referred to as the spectral complexity and spatial complexity, respectively. Without POD filtering, attempts to apply DMD to the raw velocity snapshot data obtained from PIV resulted in a complexity mismatch where $N < M$; this situation also occurs for small values of the truncation parameter ($\epsilon_t < 1\%$). Above a truncation threshold of approximately 1%, which varied slightly for each swirl number considered, the spectral and spatial complexity of the resulting DMD modes was no longer mismatched. Thus, the lower limit for ϵ_t was set by the value at which the spectral and spatial complexities are approximately matched, *i.e.*, $N \approx M$.

To determine a set threshold for each swirl number considered, a balance was struck between practical analytical considerations and energy retention. Generally, for the same value

of ϵ_t , jets with higher swirl number require more modes to capture the same fraction of fluctuating energy. This is due to the increasingly complex dynamics that appear as swirl is increased. Thus, a single threshold could not be selected for all cases. Instead, a value for the truncation parameter was selected for each of the three flow regimes identified during preliminary analysis, which is discussed further in Chapter 4. This ensures that the two cases within each regime maintain approximately the same number of modes and that motions that may be present in one case are not filtered out completely in another case in the same flow regime. The values selected for ϵ_t are listed in Table 2.

Table 2. Swirl numbers and corresponding DMD truncation parameters.

Geometric Swirl Number	Truncation Parameter (%)
0.00	3.5
0.18	
0.38	6
0.46	
0.56	10
0.66	

3.3 Validation

To validate and better understand the DMD algorithm, synthetic flow field data were generated by simulating the propagation of waves through a fluid. This was done by simulating the inviscid form of Burgers' equation using MATLAB. Burgers' equation is a one-dimensional simplification of the Navier-Stokes equations found by assuming that there are no pressure gradients in the flow, the flow is incompressible, and gravitational effects are negligible. These assumptions lead to a nonlinear partial differential equation for velocity, u , as a function of time, t , and position, x [23]:

$$\frac{\partial u}{\partial t} + u \frac{\partial u}{\partial x} = \mu \frac{\partial^2 u}{\partial x^2}. \quad (3.15)$$

For simplicity, the simulated fluid was assumed to be inviscid ($\mu = 0$), leading to the inviscid form of Burgers' equation:

$$\frac{\partial u}{\partial t} + u \frac{\partial u}{\partial x} = 0. \quad (3.16)$$

To write the equation in a more familiar form, a substitution can be conducted using

$$f(u) = \frac{1}{2}u^2 \quad (3.17)$$

Which, when substituted into Equation 3.16, yields a form recognizable as a hyperbolic conservation law [23]:

$$\frac{\partial u}{\partial t} + \frac{\partial f(u)}{\partial x} = 0. \quad (3.18)$$

This equation was solved numerically using a two-step finite difference method known as the MacCormack method. This two-step finite difference method uses a forward difference prediction step and a backward difference correction step, thereby achieving second-order accuracy [24]. In the following discussion of the solution scheme, subscripts represent spatial nodes and superscripts represent time steps. First, a prediction of the next time step is calculated using a forward difference:

$$u_j^* = u_j^n - \frac{\Delta t}{\Delta x} [f(u_{j+1}^n) - f(u_j^n)], \quad (3.19)$$

where n and j are the current time step and spatial node, respectively, Δt is the time interval covered in each step, and Δx is the size of each spatial discretization. This prediction is corrected using a backward difference to calculate the actual velocity at the next time step:

$$u_j^{n+1} = \frac{1}{2} (u_j^n + u_j^*) - \frac{1}{2} \frac{\Delta t}{\Delta x} [f(u_j^*) - f(u_{j-1}^*)]. \quad (3.20)$$

To match the experimental data, each simulation was run using 100 streamwise nodes and 51 cross-stream nodes. The time step was specified as $\Delta t = 0.2$ ms in order to match the time between PIV snapshots, and each simulation ran for 5000 timesteps to generate an equivalent number of frames as in each set of experimental data. At the start of each simulation, the velocity at each node was set to a value of $\bar{u} = 28$ m/s to match the bulk velocity of the actual jet. The spacing between nodes was held constant at a value of $\Delta x = \bar{u}\Delta t$. To generate flow features that DMD would be able to identify, the flow “inlet” was periodically perturbed with sinusoidal disturbances at various frequencies ω_i , amplitudes ϵ_i , and growth rates γ_i .

Mathematically, the inlet boundary condition is given as Equation 3.21:

$$u(0, t) = \bar{u} + \sum_i \epsilon_i \exp(\gamma_i t) \sin(\omega_i t). \quad (3.21)$$

Prior to any specific validation tests, the proper truncation parameter was selected. Unlike the truncation of experimental data as discussed above, the proper truncation parameter was much more obvious when analyzing the synthetic data. In all of the synthetic cases, the singular values produced by the SVD in the POD-filtering step discussed above suggest a clear cutoff point. In the case of the single wave used to validate the growth rate as discussed below, this cutoff was between the 100th singular value, which was on the order of 10^{-2} , and the 101st singular value, which was on the order of 10^{-10} . Clearly, the first 100 POD modes contained the vast majority of the fluctuating kinetic energy and the remaining modes were filtered out prior to the application of DMD. This behavior was similar in the multi-wave cases discussed below, though the number of modes retained was greater due to the increased complexity of the flow field due to the additional disturbances.

To validate the performance of the DMD algorithm, a number of test schemes were developed. First, a simulated flow field containing ten waves at frequencies from 100 Hz to

1000 Hz in 100 Hz increments was tested. These disturbances each had growth rates of zero and were tested a range of individual amplitudes from 0.001 m/s to 0.03 m/s. Both with and without Gaussian noise applied to the synthetic data, the DMD algorithm was able to identify wavelike motion in the flow and produced frequencies accurate to within ± 0.1 Hz. Sample mode shapes are shown in Figure 6 for 100 Hz and 300 Hz motions. While the DMD algorithm accurately identified mode shapes and frequencies, the amplitude of each mode was not accurately calculated. This is due to the fact that the algorithm specified above calculates an initial mode amplitude at $t = 0$ s. Under the current simulation conditions, the flow is initially unperturbed, resulting in an initial amplitude of zero for each motion. Notably, while the algorithm did not calculate the amplitudes specified as ϵ_i in Equation 3.21, it did calculate initial amplitudes close to zero (on the order of 10^{-5} m/s for each mode), which still reflects the simulated data. Additionally, the growth rates calculated by the algorithm are negligible for each mode (on the order of 10^{-7} m/s²), which accurately reflects the specified growth rates of zero for each perturbation.

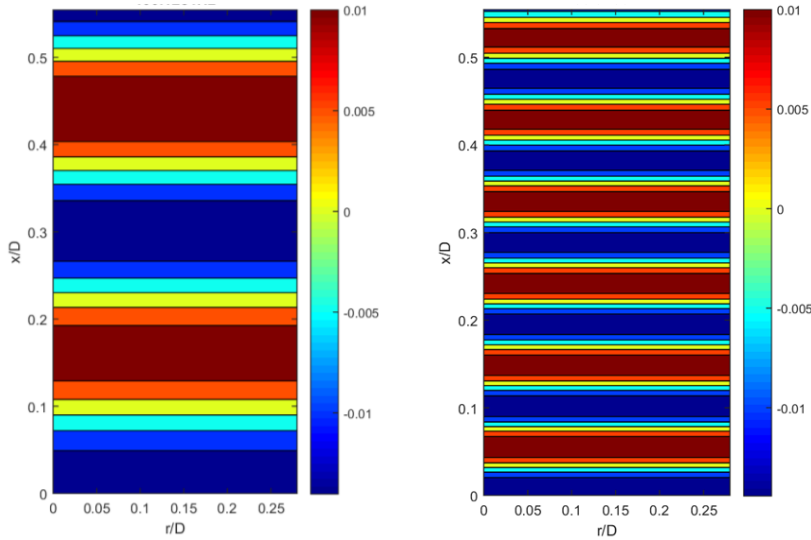


Figure 6. Sample mode shapes for a) 100 Hz and b) 300 Hz modes from the first validation test without Gaussian noise.

These validation cases were also used to understand how to analyze the growth rates/frequency pairs produced by the DMD algorithm. To generate a mode “spectrum,” growth rate is plotted against frequency for each mode. The spectrum for the validation data discussed above without Gaussian noise is given in Figure 7. The dot color in Figure 7 is representative of the initial mode amplitude, b , as calculated in Equation 3.14. The only mode with a non-negligible initial amplitude is the mode representing the mean flow, found at a frequency of 0 Hz. Generally, modes with the highest growth rates contain the most “important” dynamics, as these motions will grow the fastest and come to dominate the flow field. Thus, it is reasonable that the waves generated by the prescribed perturbations all lie on the top of the spectrum, as they are the dominant structures in the flow. Notably, the plot in Figure 7 does not contain the full set of modes produced by the algorithm. Due to the nonlinear nature of Burgers’ equation, the spectrum also contains harmonics of the prescribed perturbation frequencies, which could be seen if the plot was extended past 1000 Hz. It is not currently known why the 100 Hz mode circled in Figure 7 has a slightly more negative growth rate than the other modes corresponding to the prescribed forcing frequencies, though it is possibly due to the smaller number of cycles of the 100 Hz motion present in the 5000 frames of validation data. The modes not corresponding to the prescribed wave disturbances contain motions concentrated at the edges of the simulation. This suggests that they contain nonlinear edge effects that are artifacts of the solution scheme, not physical motions.

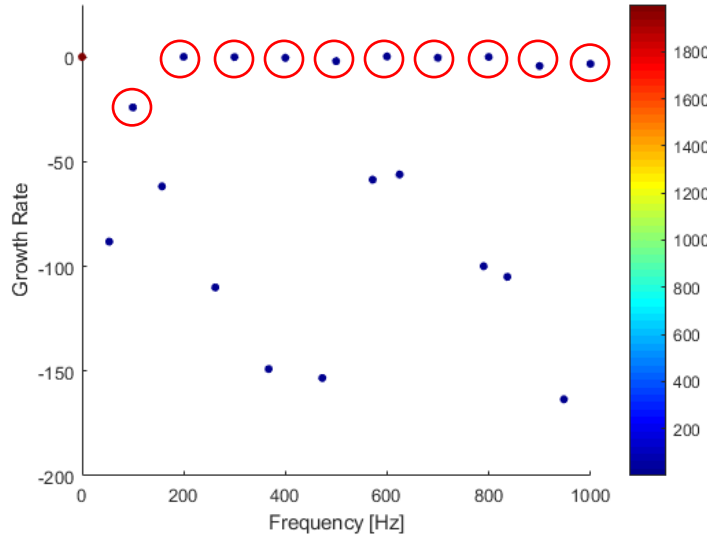


Figure 7. DMD spectrum for first validation case without Gaussian noise. Circles indicate modes at the prescribed perturbation frequencies.

To understand the behavior of the DMD algorithm when motions are growing or decaying, a range of tests were run at various growth rates. These tests were conducted using a single perturbation at 800 Hz with an initial amplitude of 0.03 m/s for cases in which the motion grew and 0.3 m/s for cases in which the motion decayed. In each case, a growth rate of either 1 m/s² or -1 m/s² was specified. In both the purely growing and purely decaying cases, the algorithm was able to capture the growth rates to within ± 0.01 m/s² without any loss in accuracy in calculating the frequencies as compared to the neutral perturbations described above. To understand the effects of a motion both growing and decaying, several cases were tested in which the 800 Hz perturbation grew and decayed in various combinations throughout the simulated dataset. These tests included:

- growing for half of the dataset, then decaying, and vice versa,
- growing for three quarters of the dataset, then decaying, and vice versa,
- alternating between growth and decay every 100 time steps.

While the mode shape and frequency were both determined to the same level of accuracy as in all other tests, the mix of growth and decay significantly affected the ability of the algorithm to calculate a growth rate. In all cases, the growth rates produced by the DMD algorithm were negative, even for the case that grew more than it decayed. In addition, there was no clear correlation between the magnitudes of the calculated growth rates and the amount of time the perturbation decayed. For example, even though the half-growing and half-decaying case and the alternating case both decayed for an equivalent number of time steps, the algorithm produced a growth rate of -0.88 m/s^2 for the former and -14 m/s^2 for the latter. As there appeared to be no relationship between the growth rates calculated between different cases, it was concluded that no quantitative analysis could be conducted on the growth rates themselves. Instead, the values were taken as qualitative indicators of modal activity, which will be discussed further in Chapter 5.

Chapter 4

Time-Averaged Results

The six swirl numbers examined in this work were selected in order to understand the behavior of vortex breakdown as it forms and eventually dominates the structure of the swirling jet. Generally, the non-swirling jet ($S = 0$) is used as a baseline with which to compare the behavior of the swirling jets. As swirl is added to the jet, vortex breakdown begins to manifest as a region of diminished axial velocity in the center of the jet. As can be seen in the time-averaged axial flow fields presented in Figure 8, this region grows in size and travels upstream as the level of swirl is increased. At intermediate levels of swirl, *i.e.*, $S = 0.38$ and 0.46 , a region of stagnation intermittently forms in the flow field. In Figure 8, this appears as a time-averaged velocity deficit along the jet centerline that increases with swirl number. At the highest swirl number considered in this study, $S = 0.66$, time-averaged stagnation is visible and vortex breakdown fully and consistently dominates the flow field along the centerline.

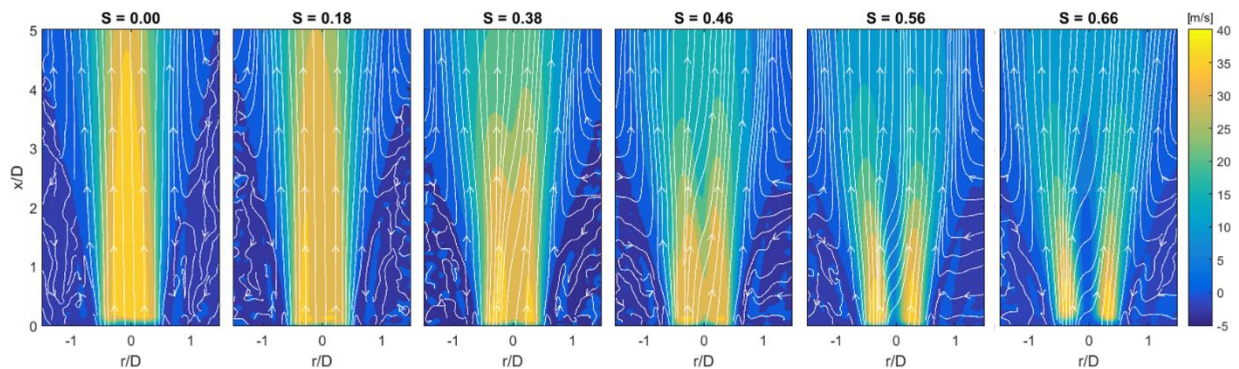


Figure 8. Time-averaged axial velocity fields for each swirl number of interest.

The axial velocity deficit that forms with increasing swirl number is better visualized in the time-averaged axial velocity profiles in Figure 9. At $S = 0$, the axial velocity profile is relatively flat, peaking at the jet centerline. As the level of swirl increases, the profile becomes bimodal, peaking on either side of the centerline. The centerline velocity deficit continues to increase as swirl increases. Notably, this deficit increases significantly between $S = 0.46$ and 0.56 , suggesting the emergence of a strong stagnation region consistent with vortex breakdown. At $S = 0.66$, the average axial velocity along the centerline is near zero, indicating the onset of time-averaged stagnation and the consistent presence of vortex breakdown in the jet.

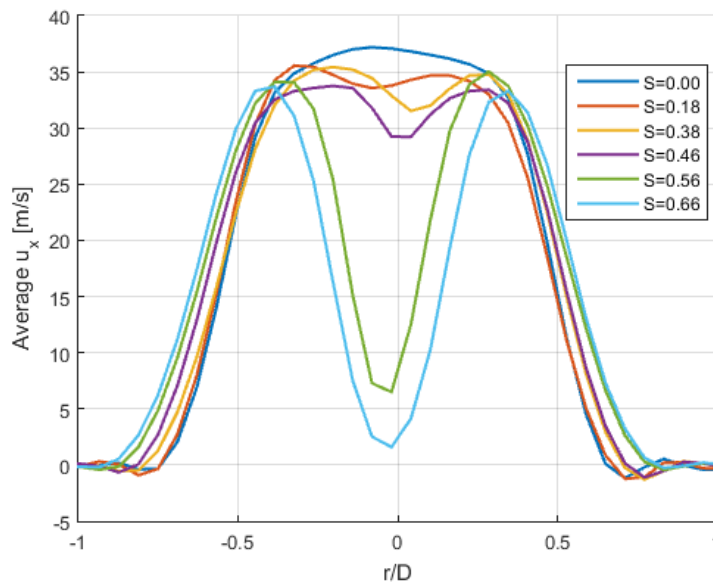


Figure 9. Average axial velocity profiles for swirl numbers of interest at $x/D = 1$.

The onset of vortex breakdown can also be visualized in the time-averaged vorticity fields presented in Figure 10. Shear layers can be identified in these fields as regions of strongly positive or negative vorticity. At $S = 0$, only a single shear layer is present around the outside of the jet. As swirl is increased to $S = 0.18$ and $S = 0.38$, the time-averaged fields suggest the

development of an inner shear layer along the centerline of the jet. At $S = 0.46$, small regions of increased vorticity appear around $x/D = 2.5$, around the same location as the time-averaged stagnation region appearing at the same swirl number in Figure 8. For higher swirl numbers, $S = 0.56$ and $S = 0.66$, the central shear layer is clear and developed, just as the stagnation region visible in Figure 8, with vorticity magnitudes comparable to those in the outer shear layer.

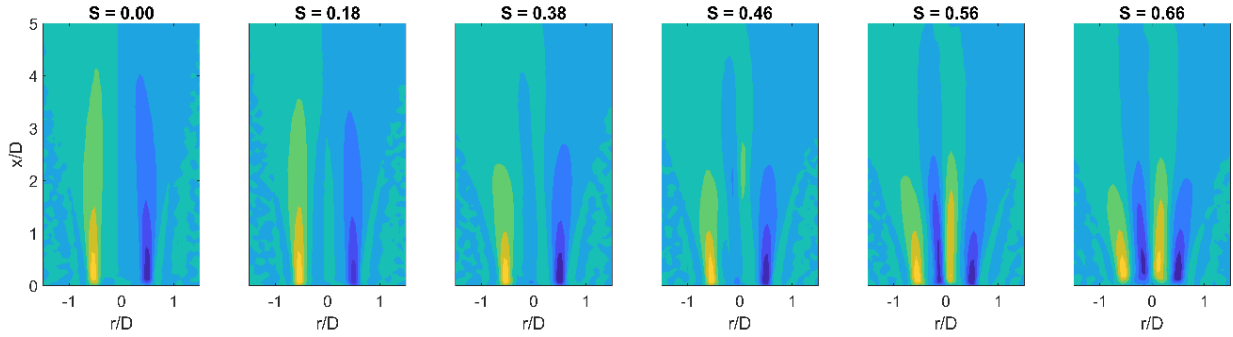


Figure 10. Time-averaged azimuthal vorticity fields for each swirl number.

Based on the properties of the time-averaged flow, further analysis is broken up into three regimes. Jets for which $0 \leq S < 0.38$ are categorized as ‘pre-breakdown,’ as the time-averaged effects of vortex breakdown are slight. Jets within the range $0.38 \leq S < 0.56$ are categorized as ‘near-breakdown.’ For these values of S , the effects of vortex breakdown are readily apparent in the time-averaged flow fields and profiles, particularly in the centerline velocity deficit illustrated in Figure 9. Finally, jets with $S \geq 0.56$ are categorized as ‘post-breakdown’ due to the dominance of vortex breakdown in the flow field and the time-averaged presence of stagnated flow and a central shear layer.

Chapter 5

Flow Dynamics

The temporal growth rates provided by DMD allow for the classification of modes as stable or unstable. To characterize the results of DMD, mode spectra such as those found in Figure 11 are generated. These spectra allow for the identification of particularly unstable modes that may lend further insight into the flow processes taking place. Notably, the growth rates of all modes considered are negative. This is likely due to averaging effects, as the timescales of the modal dynamics are much shorter than the PIV time series from which the modes are extracted. While no quantitative results can be drawn from the resulting growth rates, modes can still be identified as more or less stable based on their relative position in the spectrum. Modes that seem to be local outliers, especially those with larger growth rates, are of particular interest, as it is these modes that dominate the flow field. One such local outlier is the mean flow field, which appears in every mode spectrum with a frequency of 0 Hz and a growth rate near zero. Unlike with POD, the mean cannot be subtracted from each velocity snapshot prior to applying DMD. While the same mode shapes and frequencies will be identified if the mean is removed, all corresponding growth rates will be zero and stability information will be lost.

Another criterion used to evaluate the DMD modes is a measure of coherence calculated by projecting each dynamic mode onto the POD basis found during the POD filtering process. This coherence value is shown as the coloring of the points plotted in the mode spectra. Modes with high coherence (in red) contain large-scale, energetic structures while those with low coherence (in blue) contain small-scale structures that are less energetic. As Schmid notes,

however, dynamic modes with a small value of the projection onto the POD basis can still represent dynamically important motions [18].

5.1 Pre-Breakdown Regime

The mode spectra for the swirl numbers analyzed in the pre-breakdown regime are shown in Figure 11. The notable modes identified for $S = 0$ largely contain axisymmetric behavior similar to that shown in Figure 12a, as is characteristic of non-swirling jets [5]. Vortex rings formed by the axial Kelvin-Helmholtz instability are found at a wide range of frequencies, notably at 734 Hz, as shown in Figure 12b. The pairing of these vortices as they convect away from the nozzle results in the larger-scale motions found in modes with lower frequency (not shown). This behavior is also seen at $S = 0.18$ but is complicated by the presence of swirl. As swirl is added to the jet, these vortex rings tilt, particularly farther downstream. This can be seen in Figure 13.

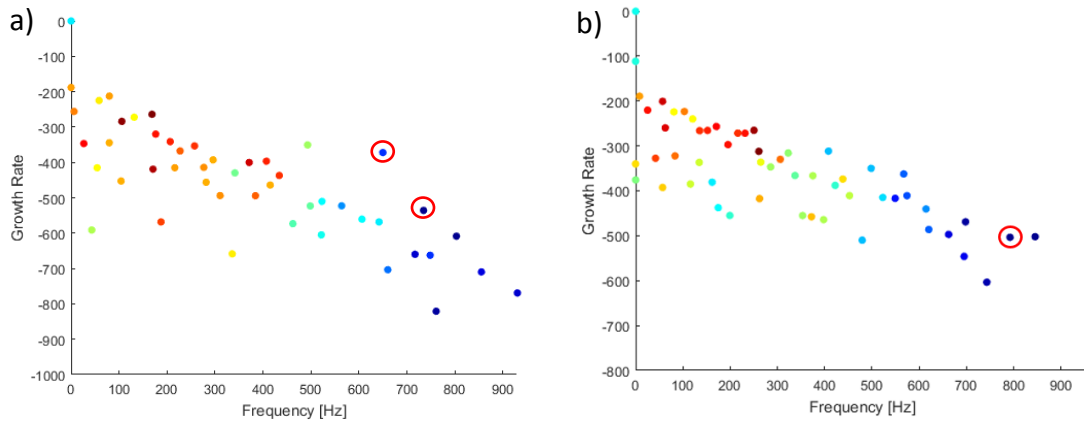


Figure 11. DMD mode spectra for a) $S = 0$ and b) $S = 0.18$. Dot color is representative of mode coherence. Circled modes are shown in Figure 12 and Figure 13.

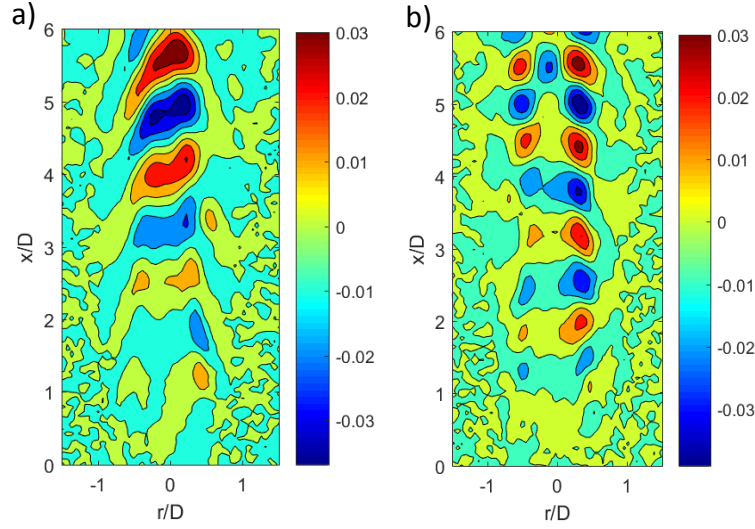


Figure 12. Notable axial modes for $S = 0$ showing a) axisymmetric behavior at 650 Hz and b) axial vortex roll-up at 735 Hz.

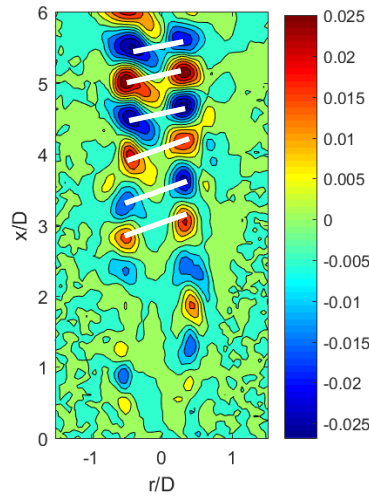


Figure 13. 792 Hz mode showing the tilting of axial Kelvin-Helmholtz vortices due to introduction of swirl at $S = 0.18$. White lines connect the centers of corresponding vortices.

5.2 Near-Breakdown Regime

As swirl is increased into the near-breakdown regime, the jet approaches the onset of vortex breakdown. This is characterized by an increase in intermittent behavior. To understand the general nature of the fluctuations present in the flow field, outlier events in axial velocity are

considered in Figure 14 for $S = 0.38$. This analysis, and all such fluctuation analysis, was conducted by Dr. Jacques Lewalle in coordination with work done for this thesis. Figure 14 contains x - r - t isosurfaces of fluctuations exceeding a set threshold (65% of bulk velocity in Figure 14a, 30% in Figure 14b, and 50% in Figure 14c) projected onto the r - x plane. Multiple occurrences at the same location are thus superposed, corresponding to higher color saturation. All fluctuations identified in Figure 14 are concentrated in the same regions of high vorticity magnitude identified in Figure 10, suggesting that these fluctuations are vortical. The strongest fluctuations, plotted in Figure 14a, are found in both the outer shear layer and the developing inner shear layer along the jet centerline. The lower-frequency fluctuations in Figure 14b are only present in the outer shear layer above approximately $x/D = 1.5$. These fluctuations are likely the result of vortices pairing in the outer shear layer, as this results in vortical motions with a characteristic frequency lower than the initial vortices. The higher-frequency fluctuations, likely the unpaired vortices, are shown in Figure 14c. These fluctuations are concentrated farther upstream and are present both in the outer shear layer and along the centerline. The presence of both positive and negative fluctuations in radial and axial velocity along the centerline between $x/D \approx 2$ and $x/D \approx 3.5$ emphasizes the intermittent nature of vortex breakdown in this regime. The same analysis for $S = 0.46$ yields similar trends and thus is not shown.

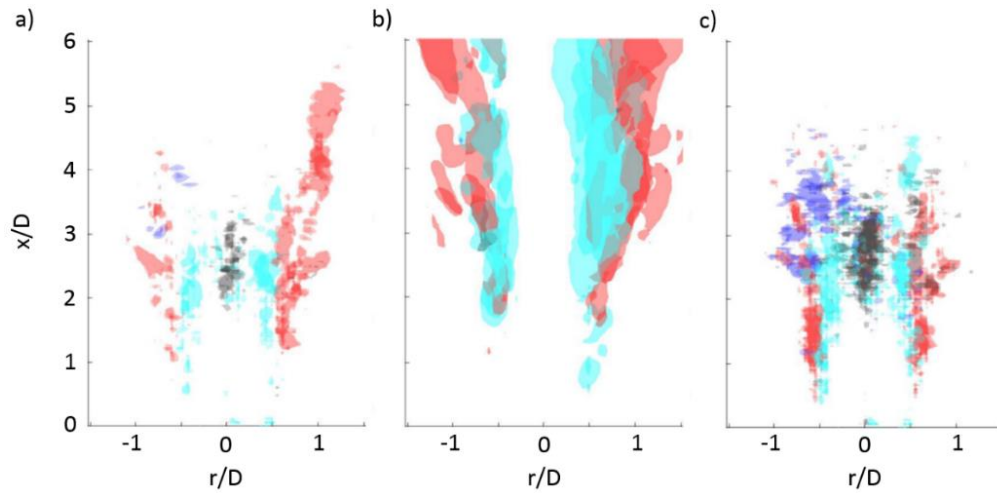


Figure 14. Axial and radial velocity fluctuations for $S = 0.38$, normalized by bulk velocity: a) unfiltered fluctuations, b) low-pass filtered with 150 Hz cutoff, and c) high-pass filtered with 150 Hz cutoff. Blue (black) coloration indicates positive (negative) radial fluctuation and red (cyan) coloration indicates positive (negative) axial fluctuation.

These fluctuations are further characterized in this regime using DMD. The DMD spectra for each near-breakdown case are shown in Figure 15. In particular, the emergence of the central velocity-deficit region characteristic of vortex breakdown is evidenced by the increased modal activity along the jet centerline across a range of frequencies at $S = 0.38$. Figure 16 illustrates the emergence of the central shear layer formed due to vortex breakdown. Upstream of $x/D = 3$, the 560 Hz mode features axisymmetric motion similar to that seen in Figure 12b in the pre-breakdown regime. Downstream of $x/D = 3$, activity shifts to the centerline of the jet, suggesting the presence of a central shear layer in which vortical structures can form. While many modes depict asymmetric activity along the centerline similar to that in Figure 16, no modes contain clear axisymmetric or antisymmetric motion. This suggests that vortex breakdown has not fully set in and that a recirculation zone has not stabilized along the centerline of the flow. At $S = 0.46$, motions along the centerline are clearer and better defined, as in Figure 17, which depicts axisymmetric motion along the centerline taking place at a frequency of 265 Hz. To better illustrate the distinction between modal activity in the outer shear layer and activity in the inner

shear layer, the time-averaged locations of maximum/minimum vorticity are overlaid on the mode in Figure 17. These locations correspond to the shear layers, with the leftmost and rightmost lines indicating the outer shear layer and the central lines indicating the inner shear layer. Both axisymmetric motions, as in Figure 17, and antisymmetric motions (not shown) appear along the centerline, suggest the onset of a more stable and consistent recirculation zone as compared to $S = 0.46$.

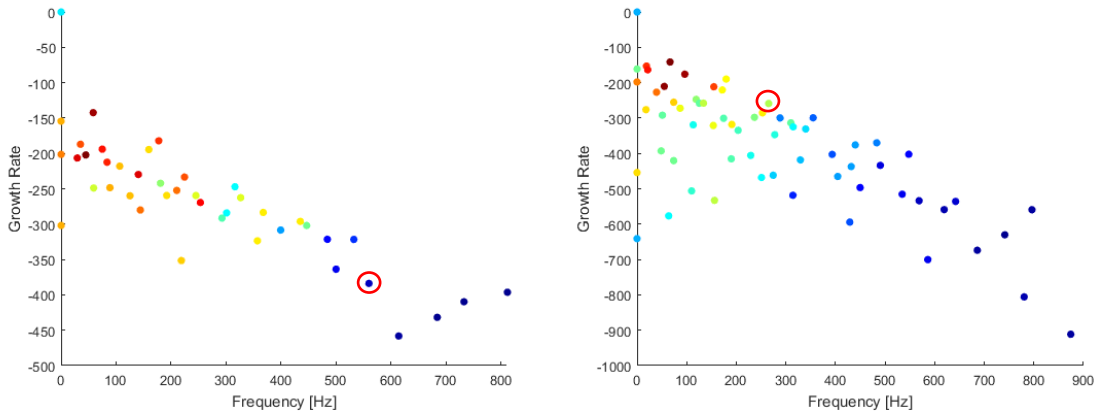


Figure 15. DMD modes for a) $S = 0.38$ and b) $S = 0.46$. Circled modes shown in Figure 11 and Figure 10.

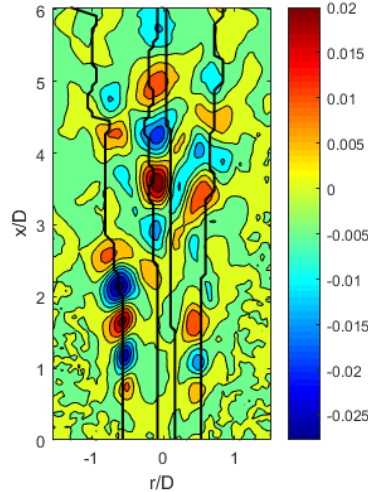


Figure 16. 560 Hz mode showing the emergence of central shear layer at $S = 0.38$.

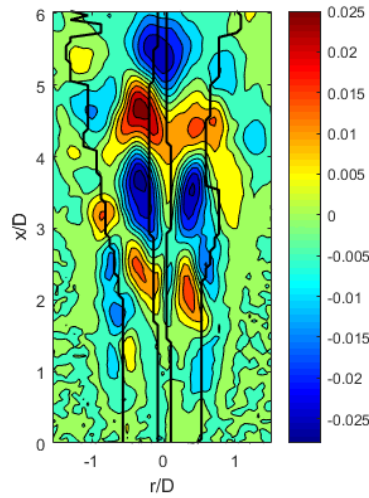


Figure 17. Coherent axisymmetric response at 265 Hz at $S = 0.46$.

Independently of the DMD decomposition, information was extracted from the azimuthal and radial velocities related to the dynamics of the vortex core. This core-tracking analysis, like the fluctuation analysis, was conducted by Dr. Jacques Lewalle in coordination with the DMD work done for this thesis. The starting point is the observation of a significant mean radial velocity along the axis of the jet, as seen in Figure 18. These velocities were interpreted as being the result of the vortex core being outside the plane of the PIV measurements. This hypothesis leads to the azimuthal component (swirl) appearing along the y-direction in the PIV plane.

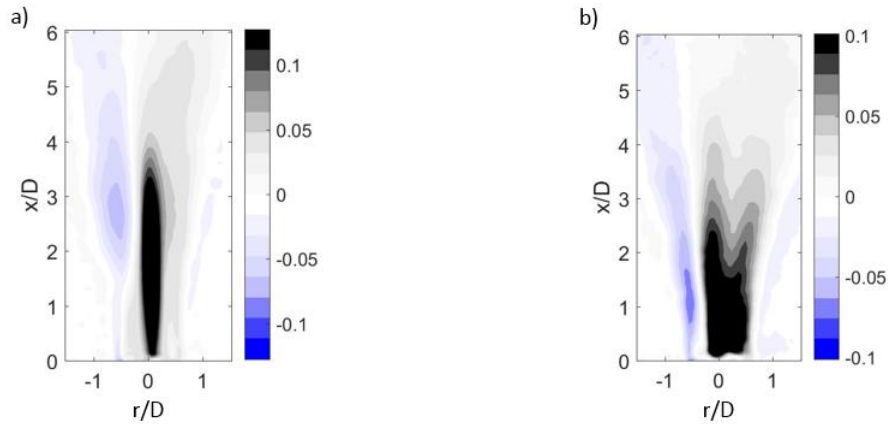


Figure 18. Examples of mean radial velocity distributions: a) $S = 0.46$, b) $S = 0.66$.

This hypothesis was used to identify a vortex core location. A vortex with its axis parallel to the plane of measurements will have two components at any given point: along the r axis (“radial”) and along the z axis (“azimuthal”). For an ideal steady line vortex, the velocity would be tangential around the vortex axis, with magnitude varying with distance from the axis. Using a Rankine vortex model, *i.e.*, a rigid-body vortex core surrounded by inviscid induced motion, two velocity vectors identify the vortex axis location at the intersection of the lines normal to the velocity. Because of measurement uncertainties and ambient turbulence, a best fit was calculated for core location using two coordinates, r and z , and rotation speed based on vectors at small $|r|$. In a first attempt, the fit was calculated based on the seven points straddling the $r = 0$ line; an improved algorithm, keeping the best fit from a set of sliding four-point-windows near $r = 0$, yielded the results described below. Vortex core reconstruction was calculated at each $x/D < 3$ for successive frames. The r - x - z - t location of the vortex core was calculated, as well as the vortex strength using a rigid body model. Two representative views, at a particular instant, are shown in Figure 19 and Figure 20. The top view in Figure 19, with the axial location color-coded from blue to red, shows that the vortex core wobbles in a region centered at about $z/D = .05$, $r/D = 0$, *i.e.*, just in front of the PIV axis. In the 3D projection view shown in Figure 20, the vortex strength is color-coded from green (high rotation rate) to blue (low rotation rate); good consistency of the vortex strength along the core seems to validate the algorithm, the model, and the convergence.

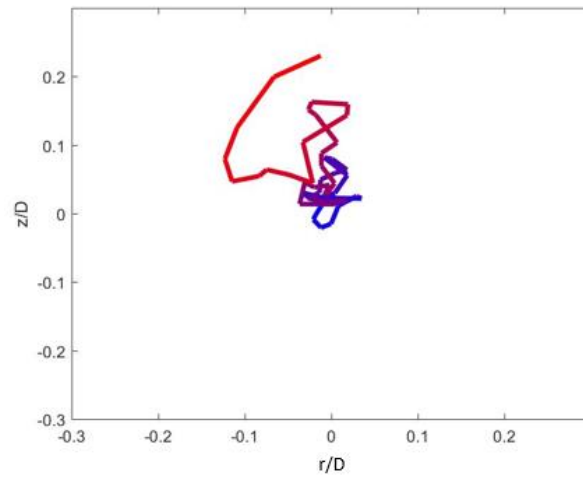


Figure 19. Top view of a snapshot of the vortex core location, blue to red denotes increasing x/D from 0 to 3.

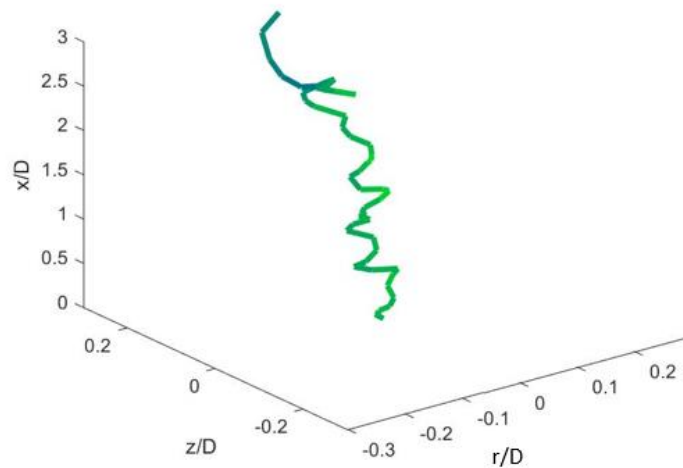


Figure 20. Perspective view of the vortex core location as for Figure 19, green to blue denotes decreasing vortex intensity.

Large excursions from the vortex center are observed mostly near the nozzle and at $x/D > 2$; these appear physically realistic, but the quality of the algorithm is likely to be less accurate at large distances from the centerline. Lack of convergence at isolated x/D levels, resulting in very large excursions from the frame of view, was skipped in the plots. It is unclear if the vortex wobble is due to buffeting by the turbulence, by vortex instability, by incomplete convergence, or a combination of such effects. Convergence of the optimization procedure at each x/D is

excellent for $S = 0.38$ and 0.46 and deteriorates significantly at larger swirl numbers. Poor convergence was diagnosed as large values of the penalty function and outlier excursions from the geometric center of the jet, and the corresponding level (x/D) was deleted from the vortex geometry. Fewer than three such points were noted for $S = 0.38$ and $S = 0.46$.

Probability distributions (pdfs) of the vortex core location were calculated for $x/D < 2.5$ over all 5000 data frames. Two representative pdfs are shown in Figure 21 for $S = 0.38$; results for $S = 0.46$ are not very different. The core location is slightly off the PIV plane, and drifts by a few millimeters at successive axial locations. The width of the distribution increases as x/D increases. This observation was made quantitative by calculating the first and second moments of the pdf, with the results shown in Figure 22. The first moments determine the mean r and z coordinates of the vortex core at each level x/D , whereas the second moment quantifies the spread of the distribution around the central point. Except for the immediate vicinity of the nozzle, the trends are very smooth. Furthermore, the trends for $S = 0.46$ and $S = 0.56$ are very similar, which gives confidence in the statistical reliability of the approach.

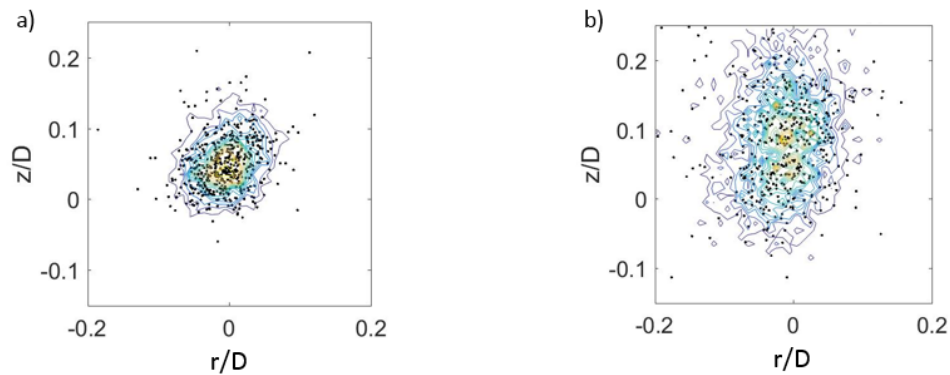


Figure 21. PDFs of vortex core locations at two axial locations: a) $x/D = 0.122$, b) $x/D = 2.316$

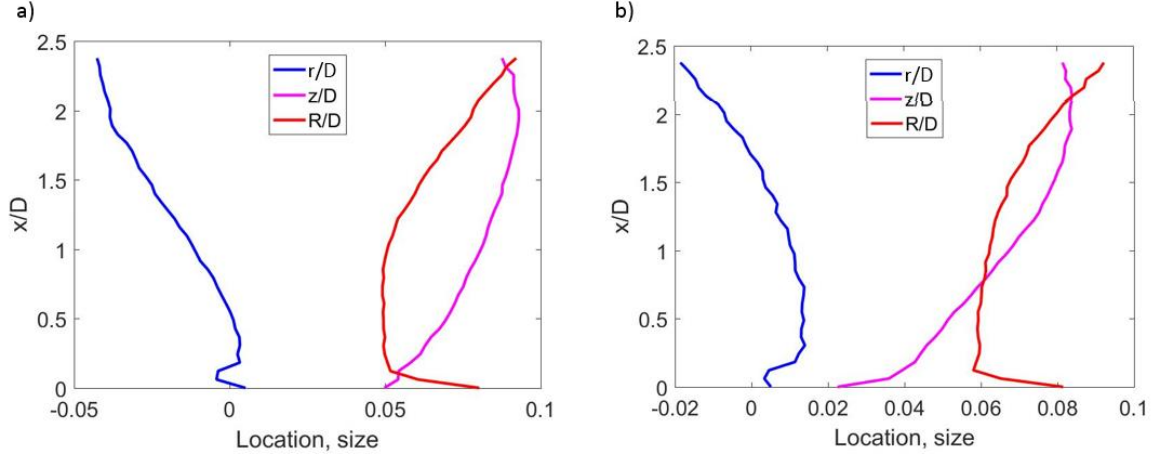


Figure 22. Mean location (r/D , z/D) and size of the vortex core (R/D) as function of axial distance (x/D): a) $S = 0.38$, and b) $S = 0.46$.

To validate the physical relevance of this vortex wobble, a point was selected on the vortex near $x/D = 0.4$ and its z -coordinate was calculated as a function of time using the Rankine vortex model. This signal was then cross-correlated with the radial velocity in the entire field via a process termed space-time cross-correlation. Figure 23 shows a sequence of snapshots of the space-time cross-correlation. The reference signal was taken as the z_c coordinate (out of the PIV plane) of the vortex core location close to the dump plane. The radial component of velocity is cross-correlated with z_c at every (r, x) point. The color scale is common to all lags. The sequence shows the propagation of fluctuations in two ways. Most obvious is the region of saturated color along the centerline near $x/D = 0$, indicating that the radial velocity is very strongly correlated with out-of-plane core location for short negative and positive lags, establishing the consistency of our analysis. It can be observed that the vortex core is slanted relative to the axis $r = 0$. There are also see weakly-correlated but slowly and consistently propagating red and grey regions along $|r/D| \approx 1$ and $x/D \approx 3$ with a sign reversal at $x/D \approx 5$ along the direction of the vortex core. This indicates an effect of vortex core motion on the entire velocity field downstream of the

reference point. A random pattern of correlations on the order of 5% measures the incomplete statistical convergence for the 5000 samples.

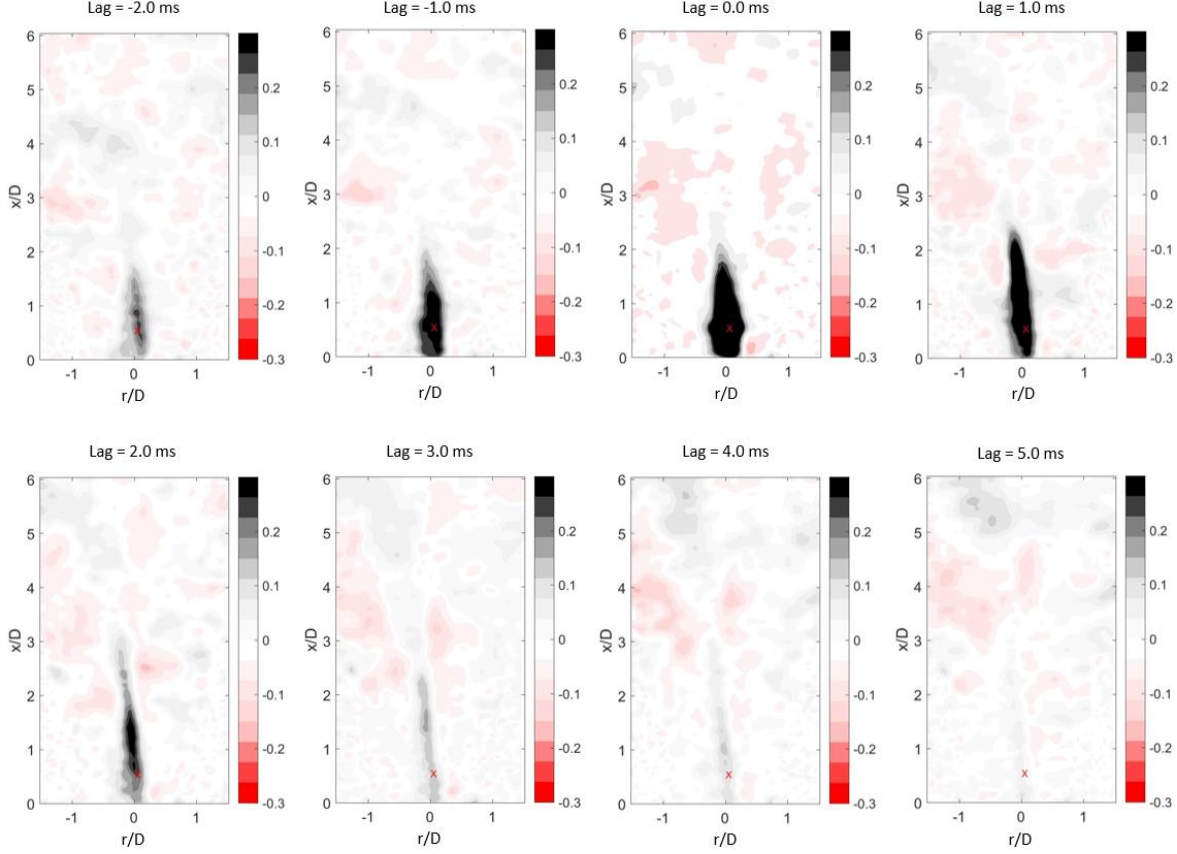


Figure 23. Cross-correlation sequence of the radial velocity field with the z -coordinate of the vortex core (reference signal) at the location marked by the red marker for $S = 0.38$. Lag increases from upper left to lower right.

5.3 Post-Breakdown Regime

As swirl is increased into the post-breakdown regime, the velocity fluctuation distributions illustrate a significant structural change. These distributions are shown in Figure 24 and use the same magnitude thresholds as those for $S = 0.38$ shown in Figure 14. The emergence of a stable central shear layer, as visualized in Figure 10, is evident in the appearance of strong axial fluctuations along the centerline in Figure 24a. However, the central shear layer has little

impact on the spatial distribution of low-frequency fluctuations, seen in Figure 24b. These fluctuations remain concentrated in the outer shear layer, though this shear layer does exhibit additional vortex spreading as compared to Figure 14b. Most notably, the jet contains significantly more high-frequency activity, shown in Figure 24b. This activity is concentrated farther upstream than at lower swirl, extending all the way to the nozzle. In addition, radial velocity fluctuations are more present than at lower swirl, suggesting a general increase in flow field fluctuation. Similar trends were found for $S = 0.66$.

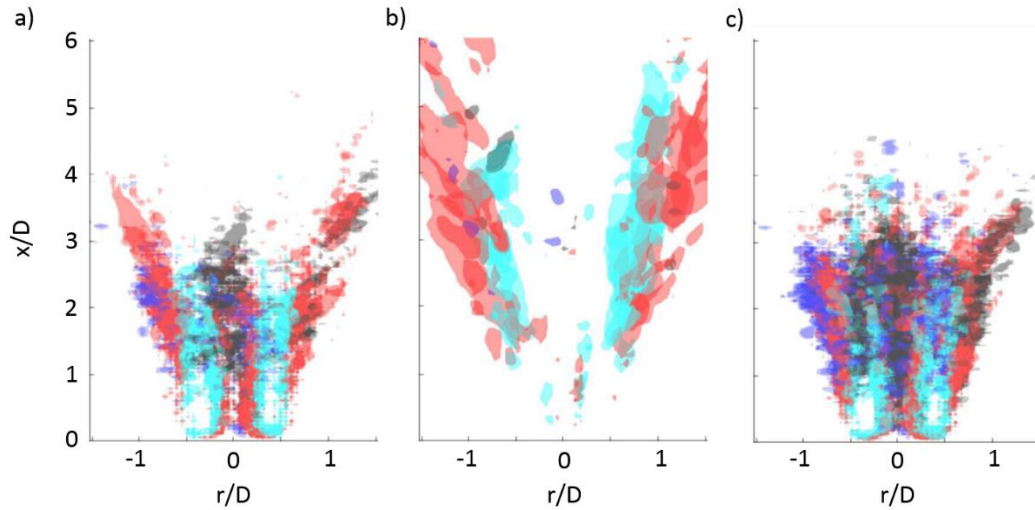


Figure 24. Axial and radial velocity fluctuations for $S = 0.56$, normalized by bulk velocity: a) unfiltered fluctuations, b) low-pass filtered with 150 Hz cutoff, and c) high-pass filtered with 150 Hz cutoff. Blue (black) coloration indicates positive (negative) radial fluctuation and red (cyan) coloration indicates positive (negative) axial fluctuation.

At $S = 0.56$, both antisymmetric and axisymmetric motions appear in both shear layers. Notably, a highly damped, antisymmetric, short length-scale motion appears at a frequency of 884 Hz. This mode manifests as a local outlier in the frequency spectrum in Figure 25a and is shown in Figure 26. A similarly-structured mode appears at a frequency just below it, at 842 Hz

(not shown). This motion is characteristic of a precessing vortex core (PVC), as has been shown in other works [16, 25]. The highly damped nature of these modes suggests that the PVC, which is a global instability, has not fully developed in the flow. At $S = 0.66$, a clearer and more coherent PVC is present in the flow at a frequency of 858 Hz. This mode is a clear local outlier in the mode spectrum in Figure 25b and is shown in Figure 27. Unlike the highly damped motion seen at $S = 0.56$, the corresponding PVC mode at $S = 0.66$ is significantly more unstable than the modes around it. Just above the dominant PVC frequency, two modes with decreasing growth rate but similar mode shape are observed. These motions are likely due to the weak nature of the PVC at this swirl number. While strong, stable PVCs manifest as limit-cycle oscillators with a single frequency, it is possible that weaker PVCs are more susceptible to fluctuating phenomenon such as turbulence. These fluctuations affect parameters such as local swirl number, which could impact the frequency of the PVC and lead to a frequency that varies in time and thus appears as multiple modes.

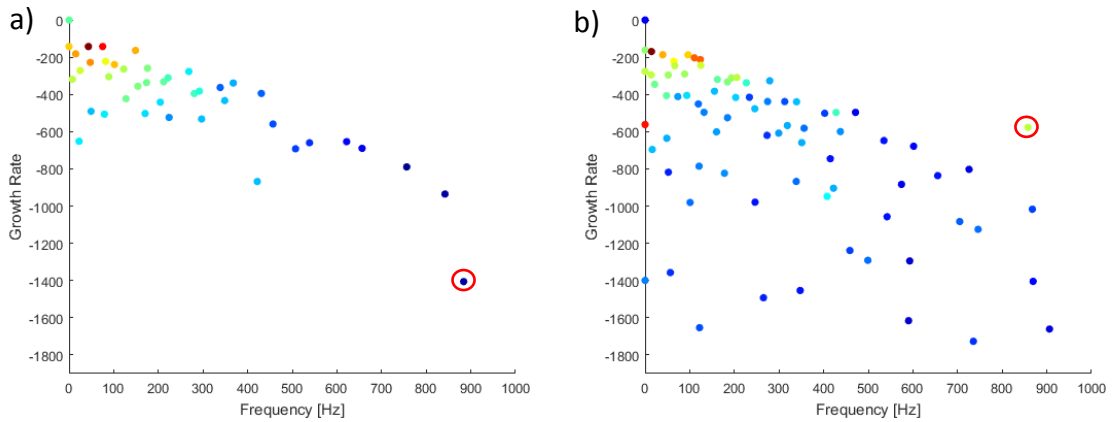


Figure 25. DMD mode spectra for a) $S = 0.56$ and b) $S = 0.66$. Circled modes are shown in Figure 26 and Figure 27.

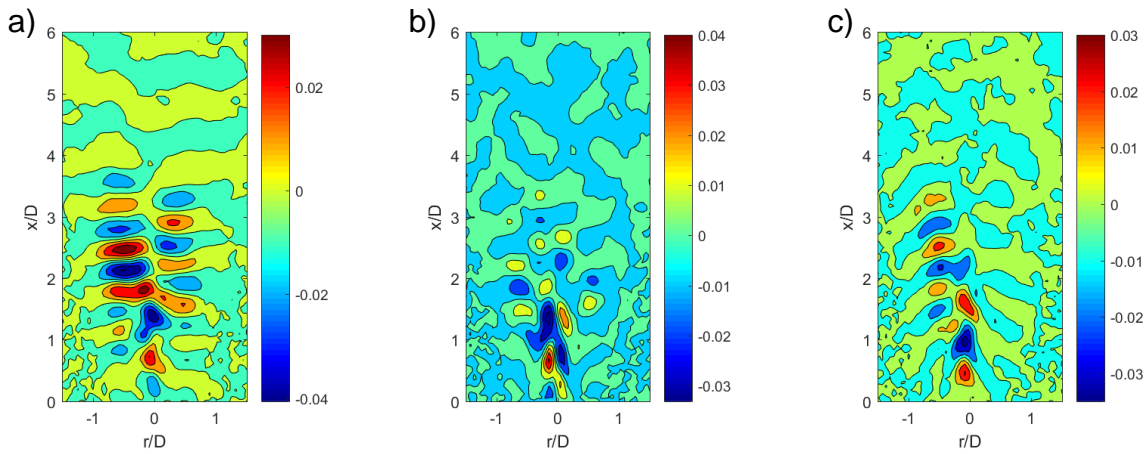


Figure 26. Emergence of highly damped PVC-like dynamics in 884 Hz mode at $S = 0.56$; a) radial mode, b) axial mode, c) azimuthal mode.

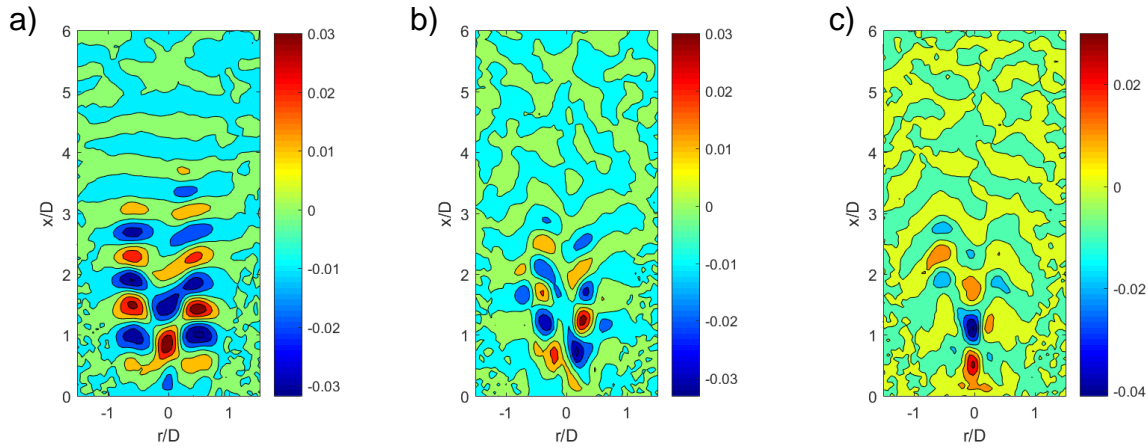


Figure 27. Clearer PVC present in 858 Hz mode at $S = 0.66$; a) radial mode, b) axial mode, c) azimuthal mode.

While DMD suggests that a weak PVC exists in the flow at $S = 0.66$, conclusions about the energy content of the PVC cannot be drawn directly from DMD. Instead, POD is used to quantify the fluctuating energy contained in the PVC motion to verify its relative strength in the flow field. As POD modes are energy-ordered, low-numbered modes are dominant in the flow field. POD modes 1 through 6 each contain between 1.3% and 2.2% of the total fluctuating

energy and capture broadband, low-frequency activity related to vortex roll-up in the shear layers. Modes 7 through 10, which each contain around 1% of the total turbulent kinetic energy, are illustrated in Figure 28 and show signs of the PVC identified using DMD in both their frequency spectra and mode shapes, which can be compared to Figure 26a and Figure 27a. The spectra of modes 7 through 10 contain wide peaks around 850 Hz, which is in general agreement with the frequency of 858 Hz identified by DMD. In addition, the mode shapes roughly correspond to those identified using DMD, suggesting that both methods have identified the same motion. The relative energy content of the PVC modes produced by POD confirms the assertion that the PVC present at $S = 0.66$ is relatively weak. Though a PVC is present at this swirl number, the flow field continues to be dominated by the vortical structures contained in POD modes 1 through 6 produced due to axial and azimuthal Kelvin-Helmholtz instability and the inertial instability caused by the rotating core.

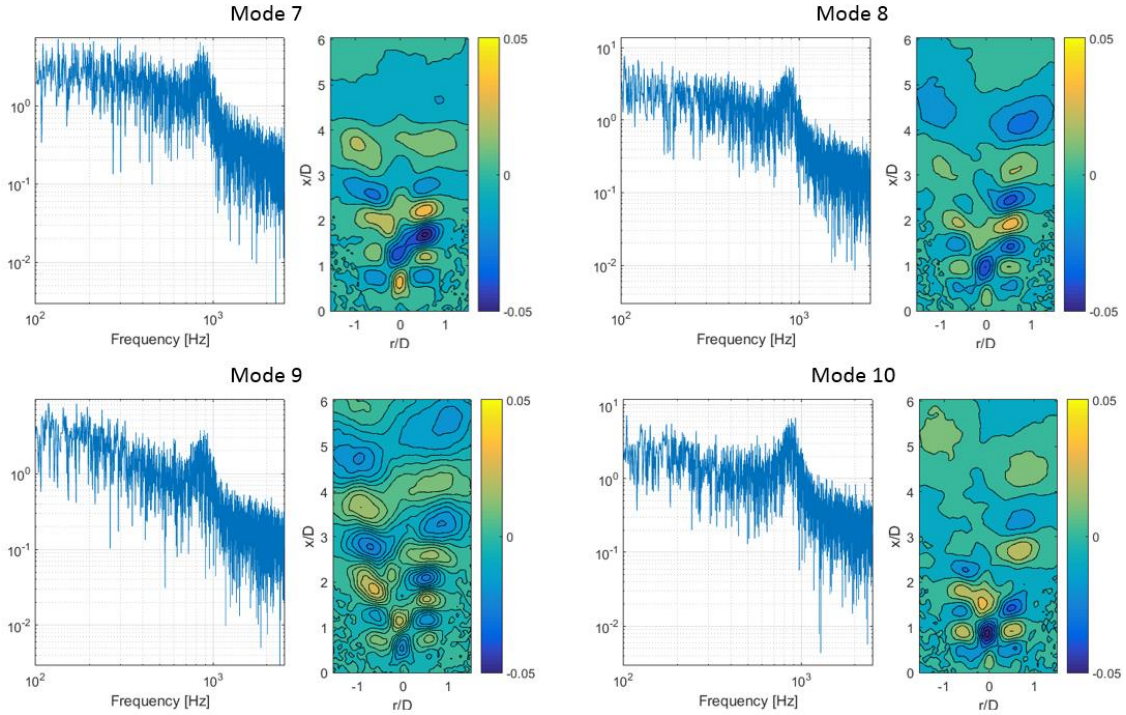


Figure 28. Radial POD modes 7-10 for $S = 0.66$.

Previous work has shown that at high swirl numbers, *i.e.*, $S > 1.05$, stronger PVCs exist than those presented in this study [16]. Strong PVCs are characterized by high amplitude, narrow band peaks in POD frequency spectra. This contrasts the broadband response of developing PVCs, as shown in Figure 28. From an energy standpoint, strong PVCs are always contained in the highest energy modes of the flow field, typically just modes one and two, which have significantly higher energy than any following modes. In previous studies using the same experimental configuration, the in-nozzle pressure transducers have been used to identify the presence of a PVC [16, 26]. At high levels of swirl, PVCs appear as narrow-band peaks in the measured pressure spectra, as indicated by the arrow in Figure 29. For $S = 0.66$, shown in red in Figure 29, no such peak can be identified despite the indication of DMD and POD that a PVC is indeed present. The small peak present in both spectra at around 1050 Hz is a system frequency present at all swirl numbers and is not indicative of a vortical motion in the flow field.

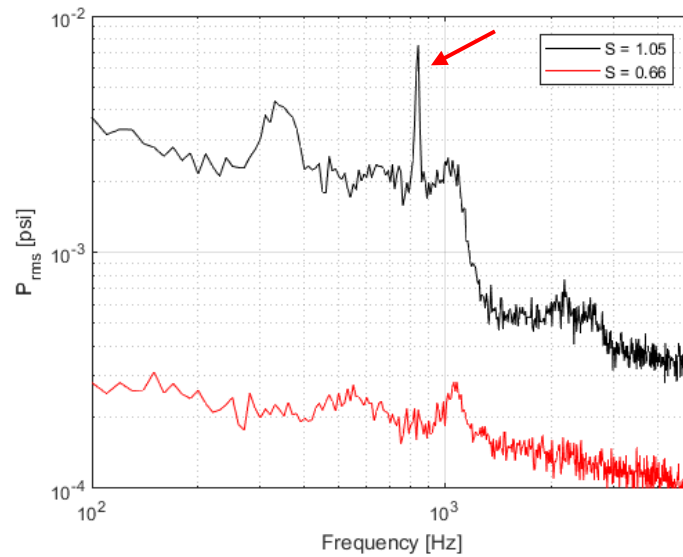


Figure 29. Pressure spectra for $S = 1.05$ case where a strong PVC is present (black) and $S = 0.66$ case featuring weak PVC (red).

Chapter 6

Conclusions and Future Work

This work has examined the dynamics of a turbulent swirling jet at a range of swirl numbers from $S = 0$ to $S = 0.66$. Three flow regimes were identified based on the presence of VB in the jet: pre-breakdown, near-breakdown, and post-breakdown. The dynamics of the jet in each regime were examined using DMD, which revealed the development of motions along the jet centerline as vortex breakdown set in in the near-breakdown regime. The dynamics identified by DMD in this turbulent study closely followed those identified in laminar studies of vortex breakdown: axisymmetric motions preceded tilting vortices, which were ultimately followed by the appearance of both axisymmetric and antisymmetric motions in a recirculation zone along the jet centerline. The location of these motions is apparent in overall analysis of strong velocity fluctuations. High-frequency fluctuations were shown to be present closer to the nozzle, while low-frequency fluctuations appear farther downstream. An apparent wobbling of the jet was also identified in the near-breakdown regime and was characterized by fitting a Rankine vortex model to the velocity fields. This wobble is not frequently discussed in swirling jet studies, and its effects could warrant further study as its presence coincides with the onset of vortex breakdown. PVC-like motions were found at a swirl number of $S = 0.56$, and a weak PVC was identified by DMD in the post-breakdown regime at a swirl number of $S = 0.66$. Its energy content was analyzed using POD.

Notably, the PVC identified by DMD was found at a significantly lower swirl number than PVCs previously identified in the same flow field. PVC-like motions were identified at a swirl number as low as $S = 0.56$, far below the point at which PVCs were observed using nozzle pressure measurements in previous studies. This suggests that in-nozzle pressure measurements are not sufficient means with which to identify weak PVCs, and that further analysis of the velocity fields is needed to confirm or deny the presence of a PVC. In particular, the DMD algorithm developed for this study is a convenient tool for this analysis due to its ability to identify single-frequency motions like PVCs. Future work will employ an improved DMD algorithm at higher swirl numbers to study the dynamics of stronger PVCs. Implementation of the higher-order DMD method used by Le Clainche and coworkers [21] could lead to the identification of additional dynamics and, generally, a more robust DMD algorithm. Additionally, future work will seek to make the growth rates produced by the current algorithm more quantitative in nature, allowing direct comparisons of mode stability between cases. Experimentally, additional tests involving dynamic bifurcation traversal could be conducted. In these dynamic cases, DMD could offer unique insight into the development of coherent structures during the onset of VB, not simply at various stages leading up to VB and following VB.

BIBLIOGRAPHY

- [1] Lefebvre, A. H. *Gas Turbine Combustion*. New York, NY: Taylor & Francis Group, 1999.
- [2] U.S. Energy Information Administration - EIA - Independent Statistics and Analysis. (n.d.). Retrieved January 18, 2018, from <https://www.eia.gov>
- [3] Billant, P., Chomaz, J.-M., and Huerre, P., "Experimental study of vortex breakdown in swirling jets," *J. Fluid Mech.* Vol. 376, 1998, pp. 183-219.
- [4] Candel, S., Durox, D., Schuller, T., Bourgouin, J., & Moeck, J. P., "Dynamics of Swirling Flames," *Ann. Rev. Fluid Mech.* Vol. 46, No. 1, 2014, pp. 147-173.
- [5] Liang, H., and Maxworthy, T., "An experimental investigation of swirling jets," *J. Fluid Mech.* Vol. 525, 2005, pp. 115-159
- [6] Gallaire, F., and Chomaz, J.-M., "Instability mechanisms in swirling flows," *Phys. Fluids* Vol. 15, 2003, pp. 2622-2639.
- [7] Peckham, D. H., and Atkinson, S. A., "Preliminary results of low speed wind tunnel tests on a Gothic wing of aspect ratio 1.0," *Aeronaut. Res. Counc.* Vol. CP 508, 1957.
- [8] Harvey, J. K., "Some observations of the vortex breakdown phenomenon," *J. Fluid Mech.* Vol. 14, No. 4, 1962, pp. 585-592.
- [9] Sarpkaya, T., "On stationary and travelling vortex breakdowns," *J. Fluid Mech.* Vol. 45, No. 03, 1971, pp. 545-559.

- [10] Sarpkaya, T., "Vortex breakdown and turbulence," *33rd Aerospace Sciences Meeting and Exhibit*, 1995.
- [11] Benjamin, T. B., "Theory of the vortex breakdown phenomenon," *J. Fluid Mech.* Vol. 14, No. 4, 1962, pp. 593-629.
- [12] Escudier, M. P., Bornstein, J., and Maxworthy, T., "The Dynamics of Confined Vortices," *Proc. R. Soc. Lond. A*, Vol. 382, No. 1783, 1982, pp. 335-360.
- [13] Healey, J. J., "Inviscid axisymmetric absolute instability of swirling jets," *J. Fluid Mech.* Vol. 613, 2008, pp. 1-33.
- [14] Loiseleux, T., Chomaz, J.-M., and Huerre, P., "The effect of swirl on jets and wakes: Linear instability of the Rankine vortex with axial flow," *Phys. Fluids* Vol. 10, 1998, pp. 1120-1134.
- [15] Rukes, L., Paschereit, C. O., and Oberleithner, K., "An assessment of turbulence models for linear hydrodynamic stability analysis of strongly swirling jets," *European Journal of Mechanics - B/Fluids*, Vol. 59, 2016, pp. 205-218.
- [16] Frederick, M., Manoharan, K., Dudash, J., Brubaker, B., Hemchandra, S., and O'Connor, J., "Impact of Precessing Vortex Core Dynamics on Shear Layer Response in a Swirling Jet," *Journal of Engineering for Gas Turbines and Power*, Vol. 140, No. 6, 2018.
- [17] Oberleithner, K., Sieber, M., Nayeri, C. N., Paschereit, C. O., Petz, C., Hege, H., . . . Wygnanski, I., "Three-dimensional coherent structures in a swirling jet undergoing vortex breakdown: Stability analysis and empirical mode construction," *J. Fluid Mech.*, Vol. 679, 2011, pp. 383-414.
- [18] Schmid, P. J., "Dynamic mode decomposition of numerical and experimental data," *J. Fluid Mech.* Vol. 656, 2010, pp. 5-28.

- [19] Schmid, P. J., "Application of the dynamic mode decomposition to experimental data," *Exp. Fluids*, Vol. 50, No. 4, 2011, pp. 1123-1130.
- [20] Kutz, J. N., Brunton, S. L., Luchtenburg, D. M., Rowley, C. W., & Tu, J. H., "On dynamic mode decomposition: Theory and applications," *Journal of Computational Dynamics*, Vol. 1, No. 2, 2014, pp.391-421.
- [21] Le Clainche, S., and Vega, J. M., "Higher order dynamic mode decomposition to identify and extrapolate flow patterns," *Phys. Fluids* Vol. 29, No. 8, 2017.
- [22] Le Clainche, S., Vega, J. M., & Soria, J., "Higher order dynamic mode decomposition of noisy experimental data: The flow structure of a zero-net-mass-flux jet," *Experimental Thermal and Fluid Science*, Vol. 88, 2017, pp. 336-353.
- [23] Hopf, E., "The partial differential equation $u_t + uu_x = \mu_{xx}$," *Communications on Pure and Applied Mathematics*, Vol. 3, No. 3, 1950, pp. 201-230.
- [24] MacCormack, R. W., "The Effect of Viscosity in Hypervelocity Impact Cratering," *Frontiers of Computational Fluid Dynamics*, 2001, pp. 27-43.
- [25] Oberleithner, K., Stöhr, M., Im, S. H., Arndt, C. M., and Steinberg, A. M., "Formation and flame-induced suppression of the precessing vortex core in a swirl combustor: Experiments and linear stability analysis," *Combust. Flame* Vol. 162, No. 8, 2015, pp. 3100-3114.
- [26] Mathews, B. H., S.; O'Connor, J. "Impact of swirling flow structure on shear layer vorticity fluctuation mechanisms," *ASME Turbo Expo 2016*. Seoul, South Korea, 2016.

Appendix A

Dynamic Mode Decomposition Code

```
% Author: Sean Clees
% Last Edit: March 25, 2018
% This code runs DMD using POD preprocessing on 3-component
stereo PIV data

testcases = {'150727x'}; % list of testcase names
thresholds = [6]; % list of truncation thresholds [%]

for p = 1:length(testcases)
    for q = 1:length(thresholds)

        close all

        % load testcase
        testcase = char(testcases(p));
        load(strcat('D:\Sean\Adjusted Mat Files\170331_good\ ',
testcase, '_VectorsAdj.mat')); % for external HDD use

        % change the range to perform DMD on a subset of the
data in question, useful for testing
        jump = 1; % time steps between frames
        time_range = 1:jump:5000; % select part of time series
        x_range = 1:100; % select subregion in x
        r_range = 1:51; % select subregion in r

        % reshape input matrices based on parameters above
        vr = vr(x_range, r_range, time_range);
        vx = vx(x_range, r_range, time_range);
        vtheta = vtheta(x_range, r_range, time_range);
        x = x(x_range);
        r = r(r_range);

        %% CREATE DATA MATRICES %%
        x_size = length(x);
        r_size = length(r);
        n = r_size * x_size; % number of points of every
velocity component per snapshot
```

```

N = n .* 3; % total number of points per snapshot (* 3
because of 3 velocity components)
M = size(vx, 3); % number of snapshots
dt = 1 ./ 5000; % time between snapshots
thresh = thresholds(q); % the truncation parameter for
the current case

% reshape velocity fields s.t. each frame becomes a
column [n x M]
vr_re = reshape(vr, [n, M]);
vx_re = reshape(vx, [n, M]);
vtheta_re = reshape(vtheta, [n, M]);

% construct data matrix X [N x M]
X = zeros(N, M);
X(1:n, :) = vr_re;
X(n + 1:n * 2, :) = vx_re;
X(n * 2 + 1:N, :) = vtheta_re;

% memory management
%clear vr vx vtheta vr_re vx_re vtheta_re

% initial order reduction step
[tempU, tempE, tempV] = svd(X, 'econ');
tol = max(size(X)) * eps(max(tempE)); % mostly
unnecessary tolerance step - economy SVD should take care of
small SVs
R = sum(diag(tempE) > tol'); % count the valid SVs

singulars = diag(tempE);
tke = singulars .^ 2;

% calculate the percent tke remaining for each number of
modes retained
tke_left = zeros(length(tke) - 1, 1);
for i = 1:R - 1
    tke_left(i) = sum(tke(i+1:end));
end
tke_percent_left = 100 .* tke_left ./ sum(tke);

tokeep = sum(tke_percent_left > thresh) - 1;

% construct reduced matrices
E = diag(singulars(1:tokeep));
U = tempU(:, 1:tokeep);
V = tempV(:, 1:tokeep);

```

```

X_reduced = E * V';

% create data matrix X1, which is just columns 1 through
M-1 of X
% [N x M - 1] and data matrix X2, which is columns 2
through M of X
% [N x M - 1]
X1 = X_reduced(:, 1:M-1);
X2 = X_reduced(:, 2:M);

% memory management
%clear tempU tempE tempV singulars tke

%% DMD ALGORITHM %%
% tic
[W, A, T] = svd(X1, 'econ'); % s.t.  $X_1 = W * A * T'$ ,
economy-sized SVD used to produce square A, eliminating the 0s
% that would appear on the
diagonal of A if full SVD was used

S_ = W' * X2 * T / A; % this is S-tilde in Kutz'
notation, / is used instead of * inv() due to computational
speed

% compute e-vecs and e-vals of S_
[Y, MU] = eig(S_); % Y is a matrix of the e-vecs of S_,
MU is a diagonal matrix of the e-vals
% e-vals describe the dynamics of the
Koopman operator, e-vecs are related
% to the e-vecs of S via a simple
transformation
MUlist = diag(MU);

% transform e-vecs of S_ into e-vecs of S (according to
Tu's definitions,
% this is "projected" DMD, not "exact")
dmodes = U * W * Y;

% rewrite e-vals for convenience & calculate frequencies
evals = diag(MU);
w = log(evals) ./ dt; % this is the useful form that
gives us meaningful information
frequencies = imag(w) ./ (2 .* pi);

```

```

        % calculate initial mode amplitudes, only necessary for
reconstruction
        b_0 = dmodes \ X(:,1);

        % toc

        % memory management
clear E U V W A T Y MU S_ V E X1 X2 X_reduced

        %% PLOT E-VALS %%
        %mkdir(strcat('E:\Sean\DMD\Swirl Timeline
Analysis\',testcase,'_',num2str(thresholds),'_',num2str(time_ran
ge(end))));
        %cd(strcat('E:\Sean\DMD\Swirl Timeline
Analysis\',testcase,'_',num2str(thresholds),'_',num2str(time_ran
ge(end))));%, '\Mean Subtracted'));

        % Plot the unmapped e-vals in the complex plane
figure;
plot(real(evals), imag(evals), '.'); % in a completely
ideal case, this will look like the unit circle
xlabel('Re(eval)');
ylabel('Im(eval)');
axis equal;

        %saveas(gcf,strcat(testcase,'_DMD_evals_raw.png'),'png')
;
        %saveas(gcf,strcat(testcase,'_DMD_evals_raw.fig'),'fig')
;

        % Plot the mapped e-vals in the complex plane
figure;
plot(imag(w), real(w), '.');
xlabel('Im(eval) Logarithmically Mapped');
ylabel('Re(eval) Logarithmically Mapped');

        %saveas(gcf,strcat(testcase,'_DMD_evals_ln.png'),'png');
        %saveas(gcf,strcat(testcase,'_DMD_evals_ln.fig'),'fig');

        % Plot the mapped growth rates against frequency
figure;
plot(frequencies, real(w), '.');
xlabel('Im(eval) Logarithmically Mapped');
ylabel('Re(eval) Logarithmically Mapped');

        %saveas(gcf,strcat(testcase,'_DMD_freqs_ln.png'),'png');

```

```

    %saveas(gcf, strcat(testcase, '_DMD_freqs_ln.fig'), 'fig');

    % Make a fancy growth rate plot against frequency
    figure;
    scatter(frequencies, real(w), abs(b_0), abs(b_0),
'filled');
    xlabel('Frequency [Hz]');
    ylabel('Growth Rate');
    colorbar;
    colormap('jet');
    axis([min(frequencies) - 1, max(frequencies) + 1,
min(real(w)), max(real(w)) + 100]);

    %saveas(gcf, strcat(testcase, '_DMD_freqs_fancy.png'), 'png
');
    %saveas(gcf, strcat(testcase, '_DMD_freqs_fancy.fig'), 'fig
');

    %% DYNAMIC SPATIAL MODES %%
    % extract the mode shapes for each velocity component
    dmodes_vr = dmodes(1:n,:);
    dmodes_vx = dmodes(n + 1:n * 2,:);
    dmodes_vtheta = dmodes(n * 2 + 1:end,:);

    % reshape the modes for plotting - (mode #, x position,
r position)
    plot_vr = reshape(dmodes_vr', [size(dmodes_vr, 2),
x_size, r_size]);
    plot_vx = reshape(dmodes_vx', [size(dmodes_vx, 2),
x_size, r_size]);
    plot_vtheta = reshape(dmodes_vtheta',
[size(dmodes_vtheta, 2), x_size, r_size]);

    if size(plot_vr, 1) > 2
        %% SORT & PLOT MODES %%

        positives = find(frequencies >= 0); % identify modes
with positive, physical frequencies
        zero_freqs = find(imag(w(positives)) == 0); %
identify modes with positive frequencies and zero growth rates

        [freq_sort, freq_sort_ind] =
sort(frequencies(positives), 'ascend'); % sort by frequency
        [amp_sort, amp_sort_ind] =
sort(real(b_0(positives)), 'descend'); % sort by initial
amplitude

```



```

'active', % if there are a ton of modes, plot only the 50 most
% otherwise save everything in order of frequency
if size(dmodes, 2) > 50
    sorting = 'Highest Growth Rates';
    num_plot = 100;
else
    sorting = 'Frequency Sorted';
    num_plot = size(positives(freq_sort_ind));
end

% sort override
% sorting = '0 Frequencies'

% set topplot based on selected sorting method
switch sorting
    case 'Highest Growth Rates'
        [unstable, unstable_ind] =
sort(real(w(positives)), 'descend'); % sort by stability
        topplot = positives(unstable_ind); % most
unstable modes w/ positive frequencies
    case 'Lowest Growth Rates'
        [damped, damped_ind] =
sort(real(w(positives)), 'ascend');
        topplot = positives(damped_ind); % most
damped modes w/ positive frequencies
    case '0 Frequencies'
        topplot = positives(zero_freqs); % modes with
0 growth rate and positive frequency
    case 'Positive Frequencies'
        topplot = positives; % all modes w/ positive
frequencies
    case 'Frequency Sorted'
        topplot = positives(freq_sort_ind); % plot
from low frequency to high frequency
    case 'Highest Amplitudes'
        topplot = positives(amp_sort_ind);
    otherwise
        topplot =
positives(freq_sort_ind([320:350])); % specific mode numbers
end

% set(0, 'DefaultFigureVisible', 'off');

```

```

        %mkdir(strcat('E:\Sean\DMD\Swirl Timeline
Analysis\',testcase,'_',num2str(thresholds),'_',num2str(time_range(end)),'\','\','sorting));
        %cd(strcat('E:\Sean\DMD\Swirl Timeline
Analysis\',testcase,'_',num2str(thresholds),'_',num2str(time_range(end)),'\','\','sorting));

        upperbound = 6; % streamwise limit for mode shape
plots
        for i = 1:length(topplot)
            title2 = ['Freq: '
num2str(frequencies(topplot(i))) ', Growth Rate: '
num2str(real(w(topplot(i)))) ', Amp: '
num2str(abs(b_0(topplot(i))))];

            %% REAL %%

            % vr shape
            figure;
            contourf(r, x,
squeeze(real(plot_vr(topplot(i),:,:))));
            colormap('jet');
            xlabel('r/D');
            ylabel('x/D');
            axis equal;
            title(['Real Radial Mode Shape', 10, title2,
10]);

            axis([-1.5 1.5 0 upperbound]);
            colorbar;

            %saveas(gcf,strcat(num2str(i),'_',testcase,'_real_vr_contour.png'),'png');
            %saveas(gcf,strcat(num2str(i),'_',testcase,'_real_vr_contour.fig'),'fig');

            % vx shape
            figure;
            contourf(r, x,
squeeze(real(plot_vx(topplot(i),:,:))));
            colormap('jet');
            xlabel('r/D');
            ylabel('x/D');
            axis equal;
            title(['Real Axial Mode Shape', 10, title2,
10]);

            axis([-1.5 1.5 0 upperbound]);

```

```

        colorbar;

        %saveas(gcf, strcat(num2str(i), '_', testcase, '_real_vx_contour.png'), 'png');
        %saveas(gcf, strcat(num2str(i), '_', testcase, '_real_vx_contour.fig'), 'fig');

        close all;

        % vtheta shape
        figure;
        contourf(r, x,
squeeze(real(plot_vtheta(topplot(i), :, :)))));
        colormap('jet');
        xlabel('r/D');
        ylabel('x/D');
        axis equal;
        title(['Real Azimuthal Mode Shape', 10, title2,
10]);

        axis([-1.5 1.5 0 upperbound]);
        colorbar;

        %saveas(gcf, strcat(num2str(i), '_', testcase, '_real_vtheta_contour.png'), 'png');
        %saveas(gcf, strcat(num2str(i), '_', testcase, '_real_vtheta_contour.fig'), 'fig');

        %% IMAG %%

        %mkdir('./Imag');
        %cd('./Imag');

        % vr shape
        figure;
        contourf(r, x,
squeeze(imag(plot_vr(topplot(i), :, :)))));
        colormap('jet');
        xlabel('r/D');
        ylabel('x/D');
        axis equal;
        title(['Imaginary Radial Mode Shape', 10,
title2, 10]);

        axis([-1.5 1.5 0 upperbound]);
        colorbar;

```

```

        %saveas(gcf,strcat(num2str(i),'_',testcase,'_ima
g_vr_contour.png'),'png');
        %saveas(gcf,strcat(num2str(i),'_',testcase,'_ima
g_vr_contour.fig'),'fig');

        % vx shape
        figure;
        contourf(r, x,
squeeze(imag(plot_vx(toplot(i),:,:))));
        colormap('jet');
        xlabel('r/D');
        ylabel('x/D');
        axis equal;
        title(['Imaginary Axial Mode Shape', 10, title2,
10]);

        axis([-1.5 1.5 0 upperbound]);
        colorbar;

        %saveas(gcf,strcat(num2str(i),'_',testcase,'_ima
g_vx_contour.png'),'png');
        %saveas(gcf,strcat(num2str(i),'_',testcase,'_ima
g_vx_contour.fig'),'fig');

        close all;

        % vtheta shape
        figure;
        contourf(r, x,
squeeze(imag(plot_vtheta(toplot(i),:,:))));
        colormap('jet');
        xlabel('r/D');
        ylabel('x/D');
        axis equal;
        title(['Imaginary Azimuthal Mode Shape', 10,
title2, 10]);

        axis([-1.5 1.5 0 upperbound]);
        colorbar;

        %saveas(gcf,strcat(num2str(i),'_',testcase,'_ima
g_vtheta_contour.png'),'png');
        %saveas(gcf,strcat(num2str(i),'_',testcase,'_ima
g_vtheta_contour.fig'),'fig');

        %cd('..');

%% PHASE %%

```

```

        %mkdir('./Phase');
        %cd('./Phase');

        % vr phase
        figure;
        contourf(r, x,
squeeze(angle(plot_vr(toplot(i),:,:)))));
        colormap('gray');
        xlabel('r/D');
        ylabel('x/D');
        axis equal;
        title(['Radial Mode Phase', 10, title2, 10]);
        colorbar;
        axis([-1.5 1.5 0 upperbound]);

        %saveas(gcf, strcat(num2str(i), '_', testcase, '_vr_
phase.png'), 'png');
        %saveas(gcf, strcat(num2str(i), '_', testcase, '_vr_
phase.fig'), 'fig');

        % vx phase
        figure;
        contourf(r, x,
squeeze(angle(plot_vx(toplot(i),:,:)))));
        colormap('gray');
        xlabel('r/D');
        ylabel('x/D');
        axis equal;
        title(['Axial Mode Phase', 10, title2, 10]);
        colorbar;
        axis([-1.5 1.5 0 upperbound]);

        %saveas(gcf, strcat(num2str(i), '_', testcase, '_vx_
phase.png'), 'png');
        %saveas(gcf, strcat(num2str(i), '_', testcase, '_vx_
phase.fig'), 'fig');

        % vtheta phase
        figure;
        contourf(r, x,
squeeze(angle(plot_vtheta(toplot(i),:,:)))));
        colormap('gray');
        xlabel('r/D');
        ylabel('x/D');
        axis equal;
        title(['Azimuthal Mode Phase', 10, title2, 10]);

```

```

        colorbar;
        axis([-1.5 1.5 0 upperbound]);

        %saveas(gcf, strcat(num2str(i), '_', testcase, '_vth
eta_phase.png'), 'png');
        %saveas(gcf, strcat(num2str(i), '_', testcase, '_vth
eta_phase.fig'), 'fig');

        close all;

        %cd('..\');
    end
end

% memory management
%clear dmodes dmodes_vr dmodes_vx plot_vr plot_vx
plot_vtheta dmodes_vtheta evals w frequencies b_0 positives
zero_freqs freq_sort freq_sort_ind amp_sort amp_sort_ind
POD_sort POD_sort_ind coherence coherence_data num_plot sorting
unstable unstable_ind damped damped_ind
    end
end

```

Appendix B

Synthetic Data Code

```
% Author: Sean Clees
% Last Edit: March 28, 2018
% This code generates simulated velocity field snapshots of a
% simple 2D
% flow field for DMD validation

%% CONSTANTS %%
frames = 5000;           % [], the number of snapshots to generate
x_dim = 100;             % [], number of streamwise nodes
r_dim = 51;              % [], number of cross-stream nodes
ubar = 28;               % [m/s], average and initial velocity
dt = 1 ./ 5000;          % [s], time step
dx = ubar .* dt;         % [m], streamwise discretization, also
% spacing between cross-stream nodes

%% PERTURBATION INFO %%
freqs = [800];           % [Hz], perturbation frequencies
amps = [0.03];           % [m/s], perturbation amplitudes
rates = [0];             % [m/s^2], perturbation growth rates

%% INITIALIZE FIELD %%
vx = zeros(x_dim, r_dim, frames);
newvx = vx(:,1);
oldvx = newvx;
vx(:, :, :) = ubar;

%% SIMULATE %%
for t = 2:frames
    oldvx = vx(:,1,t-1);
    newvx(1) = ubar + sum(exp(rates * (t - 1) .* dt) .* amps .*
sin(2 * pi * freqs * (t-1) * dt)); % + normrnd(0, 0.01); %
% uncomment normrnd part for gaussian noise

    % MacCormack O(2)
    tempvx = oldvx(1:end-1) - dt./dx .* (0.5 .*
(oldvx(2:end)) .^ 2 - 0.5 .* (oldvx(1:end-1)) .^ 2);
```

```

    newvx(2:end-1)= 0.5.*(oldvx(2:end-1) + tempvx(2:end)) -
0.5.*dt./dx.* (0.5 .* (tempvx(2:end)) .^ 2 - 0.5 .*
(tempvx(1:end-1)) .^ 2);

    % Outlet BC
    newvx(end) = 0.5 .* (oldvx(end) + newvx(end - 1));

    % copy 1D simulation across to make 2D field
    for j = 1:r_dim
        vx(:,j,t) = newvx;
    end
end

%%
% construct spatial coordinate vectors
x = dx .* (0:x_dim - 1);
r = dx .* (0:r_dim - 1);

save('validationdata1', 'r', 'x', 'vx');

% plot waves
set(0, 'DefaultFigureVisible', 'on');

for t = frames - 100:frames
    surf(r, x, squeeze(vx(:,:,t)));
    title(num2str(t));
    view([90 0]);
    colorbar;
    caxis([(ubar - sum(amps) - 0.3), (ubar + sum(amps) + 0.3)]);
    zlim([27, 29]);
    drawnow
end

```


ACADEMIC VITA

Sean Clees

sic5536@psu.edu

Education: Bachelor of Science in Nuclear Engineering with Honors in Mechanical Engineering
Expected May 2018
The Pennsylvania State University, Schreyer Honors College
Dean's List seven out of seven semesters

Honors: Schreyer Honors Scholar
2018 NSF Graduate Research Fellowship Honorable Mention
2017 Erickson Discovery Grant recipient
Penn State Provost's Award recipient
Monty Schultz Memorial Scholarship in Nuclear Engineering recipient
Pennsylvania Ready to Succeed Scholarship recipient
Spring 2015 Engineering Design 100 Showcase, Most Innovative Design winner

Engineering Experience:

Undergraduate Researcher, Penn State Reacting Flow Dynamics Laboratory (2016 – Present)

- Conduct ongoing experimental studies of gas turbine combustor flow fields using high-speed laser diagnostics
- Authored a paper presented at 2018 AIAA SciTech Forum, titled "Vortex Core Dynamics in a Swirling Jet Near Vortex Breakdown"
- Implemented advanced dimensionality-reducing analysis methods using MATLAB to study nonlinear dynamics in swirling jets
- Developed a data acquisition system using LabVIEW and cRIO hardware
- Conducted research in the summer of 2017 via an Erickson Discovery Grant

Reactor Physics Honors Option Project (2016)

- Developed MATLAB code to simulate the transport of charged particles
- Verified code with preexisting experimental databases
- Used stopping power calculations to develop a mock treatment plan for a cancer patient receiving proton therapy

Relevant Skills:

Software

- MATLAB, C++, Bash, LabVIEW, SolidWorks, DaVis 8.4, SCALE 6.2.1, Microsoft Office, Windows, Mac

Coursework

- Fluid Flow, Thermodynamics, Statistical Thermodynamics, Heat Transfer, Reactor Physics, Reactor Design and Advanced Reactor Design, Reactor Systems Analysis, Radiation Detection, Experiments in Reactor Physics, Calculus I-III, Differential Equations
- Working proficiency and minor in Spanish

Employment Experience:

Learning Assistant, Penn State Department of Mathematics (2015 – Present)

- Regularly hold small-group review sessions for introductory calculus material

Line Technician, Lutron Electronics Co. (2015 – 2016)

- Worked as a member of a team to assemble and package lighting products